

Accreting, highly magnetized neutron stars at the Eddington limit: A study of the 2016 outburst of SMC X-3

Filippos Kolliopoulos^{1,2*} and Georgios Vasilopoulos³

¹ CNRS, IRAP, 9 Av. colonel Roche, BP 44346, F-31028 Toulouse cedex 4, France

² Université de Toulouse; UPS-OMP; IRAP, Toulouse, France

³ Max-Planck-Institut für Extraterrestrische Physik, Giessenbachstrasse, 85748 Garching, Germany

Received ... / Accepted ...

ABSTRACT

Aims. To study the temporal and spectral characteristics of SMC X-3 during its recent (2016) outburst. To probe accretion onto highly magnetized neutron stars (NSs), at the Eddington limit.

Methods. We obtained *XMM-Newton* observations of SMC X-3 and combined them with long-term observations by *Swift*. We performed a detailed analysis of the temporal and spectral behavior of the source, and its short- and long-term evolution. We have also constructed a simple toy-model – albeit based on robust theoretical predictions – in order to gain insight into the complex emission pattern of SMC X-3.

Results. We confirm the pulse period of the system, derived by previous works and note that the pulse has a complex, three peaked shape. We find that the pulsed emission is dominated by hard photons, while at energies below ~ 1 keV, the emission is virtually non-pulsating. We further find that the shape of the pulse profile and the short and long-term evolution of the source light-curve can be explained by invoking a combination of a “fan” and a “polar” beam. The results of our temporal study are supported by our spectroscopic analysis, which reveals a two-component emission, comprised of a hard power law and a soft thermal component. We find that the latter produces the bulk of the non-pulsating emission and is most likely the result of reprocessing of the primary hard emission, by optically thick material that partially obscures the central source. We also detect strong emission lines from highly ionized metals. The strength of the emission lines are strongly phase-dependent.

Conclusions. Our findings are in agreement with previous works. The energy and temporal evolution and the shape of the pulse profile and the long-term spectra evolution of the source are consistent with the expected emission pattern of the accretion column in the super-critical regime, while the presence of a large reprocessing region is consistent with the analysis of previously studied X-ray pulsars observed at high accretion rates. The presence of this reprocessing region is consistent with recently proposed theoretical and observational works that suggest that highly magnetized NSs occupy a considerable fraction of ULXs.

Key words. Keywords should be given

1. Introduction

X-ray pulsars (XRPs) are comprised of a highly magnetized ($B > 10^9$ G) neutron star (NS) and a companion star that ranges from low-mass white dwarfs to massive B-type stars (e.g. Caballero & Wilms 2012; Walter et al. 2015; Walter & Ferrigno 2016, and references therein). XRPs are some of the most luminous – off nuclear – Galactic X-ray point sources (e.g. Israel et al. 2017a). The X-ray emission is the result of accretion of material from the *donor* star onto the NS, which – in the case of XRPs – is strongly affected by the NS magnetic field. Namely, the accretion disk formed by the in-falling matter from the companion star, is truncated at approximately the NS magnetosphere. From this point, the accreted material flows towards the NS magnetic poles, following the magnetic field lines, forming an *accretion column*, inside which, material is heated to high energies (e.g. Basko & Sunyaev 1975, 1976; Meszaros & Nagel 1985). The opacity inside the accretion column is dominated by scatterings between photons and electrons. In the presence of a high magnetic field – the scattering cross-section is highly anisotropic (Canuto et al. 1971; Lodenguai et al. 1974), the hard X-ray photons from the accretion column are collimated in a narrow (“pencil-”) beam, which is directed parallel to the magnetic

field axis (Basko & Sunyaev 1975). The (possible) inclination between the pulsar beam and the rotational axis of the pulsar, combined with the NS spin, produce the characteristic pulsations of the X-ray light-curve.

During episodes of prolonged accretion, XRPs are known to reach and often exceed the Eddington limit for spherical accretion onto a NS ($\sim 1.8 \times 10^{38}$ erg/s for a $1.4 M_{\odot}$ NS). This picture is further complicated by the fact that material is accreted onto a very small area on the surface of the NS, and as a result the Eddington limit is significantly lower. Therefore, even X-ray pulsars with luminosities of \sim a few 10^{37} erg/s, are persistently breaking the (local) Eddington limit. Basko & Sunyaev (1976) demonstrated that – while the accreting material is indeed impeded by the emerging radiation and the accretion column becomes opaque along the magnetic field axis – the X-ray photons can escape from the (optically thin) sides of the accretion funnel, in a “fan-beam” pattern (see e.g. Fig. 1 Schönheer et al. 2007) that is directed perpendicular to the magnetic field. More recent considerations also predict that a fraction of the fan-beam emission can be reflected off the surface of the NS, producing a secondary “polar” beam, directed parallel to the magnetic field axis (Trümper et al. 2013; Poutanen et al. 2013).

The recent discoveries of pulsating ultraluminous X-ray sources (PULXs), have established that XRPs can persistently

* e-mail: fkolliopoulos@irap.omp.eu

emit at luminosities that are hundreds of times higher than the Eddington luminosity (e.g. [Bachetti et al. 2014](#); [Fürst et al. 2016](#); [Israel et al. 2017a](#)). Indeed, refinements of the mechanism put forward by [Basko & Sunyaev \(1976\)](#), demonstrated that accreting highly magnetized NSs, can facilitate luminosities exceeding $10^{40} \text{ erg s}^{-1}$ ([Mushtukov et al. 2015](#)), while other recent studies propose that many (if not most) ULXs are accreting (highly magnetized) NSs, rather than black holes ([King & Lasota 2016](#); [King et al. 2017](#); [Pintore et al. 2017](#); [Mushtukov et al. 2017](#); [Koliopanos et al. 2017](#)).

Understanding the intricacies of the physical mechanisms that underly accretion onto high-B NSs, requires the detailed spectral and timing analysis of numerous XRP, during high accretion episodes. The shape of the pulse profile in different energy bands and at different luminosities provides valuable insights to the shape of the emission pattern of the accretion column and may also shed light on the geometry and size of the accretion column itself (e.g. [Nagel 1981](#); [White et al. 1983](#); [Mészáros 1992](#); [Paul et al. 1996, 1997](#); [Rea et al. 2004](#); [Vasilopoulos et al. 2013, 2014](#); [Koliopanos & Gilfanov 2016](#)). Furthermore, the shape of the spectral continuum, its variability and the fractional variability of the individual components of which it is comprised, along with the presence (or absence), shape and variability of emission-like features are directly related to the radiative processes that are at play in the vicinity of the accretion column, and may also reveal the presence of material trapped inside or at the boundary of the magnetosphere ([Basko 1980](#); [Sunyaev & Titarchuk 1980](#); [Schulz et al. 2002](#); [La Palombara & Mereghetti 2006](#); [Reig et al. 2012](#); [Vasilopoulos et al. 2016](#); [Vasilopoulos et al. 2017 in press](#)).

The emission of the accretion column of XRP has a spectrum that is empirically described by a very hard power law (spectral index $\lesssim 1.8$) with a low energy ($\lesssim 10 \text{ keV}$) cut-off (e.g. [Caballero & Wilms 2012](#)). It has been demonstrated that the spectrum can be reproduced assuming bulk and thermal Comptonization of bremsstrahlung, black-body and cyclotron seed photons ([Nagel 1981](#); [Mészáros & Nagel 1985](#); [Burnard et al. 1991](#); [Hickox et al. 2004](#); [Becker & Wolff 2007](#)). Nevertheless a comprehensive, self consistent modeling of the emission of the accretion column has not been achieved yet. The spectra of XRP often exhibit a distinctive spectral excess below $\sim 1 \text{ keV}$, which is successfully modeled using a black body component at a temperature of $\sim 0.1\text{--}0.2 \text{ keV}$ (e.g. [Hickox et al. 2004](#), and references therein). While some authors have argued that this “soft excess” is the result of Comptonization of seed photons from the truncated disk, by low-energy ($kT_e \lesssim 1 \text{ keV}$) electrons (e.g. [La Barbera et al. 2001](#)), others have noted that the temperature of the emitting region is hotter and its size considerably larger than what is expected for the inner edge of a truncated [Shakura & Sunyaev \(1973\)](#) accretion disk and they attribute the feature to reprocessing of hard X-rays by optically thick material, trapped at the boundary of the magnetosphere. More recently, [Mushtukov et al. \(2017\)](#) have extended these arguments to the super-Eddington regime, arguing that at high mass accretion rates (considerably above the Eddington limit) this optically thick material engulfs the entire magnetosphere and reprocesses most (or all) of the primary hard emission. The resulting accretion “curtain” is substantially hotter ($\gtrsim 1 \text{ keV}$), than that of the soft excess in the sub-Eddington sources.

Be/X-ray binaries (BeXRBs; for a recent review see [Reig 2011](#)) are a subclass of High-mass X-ray binaries (HMXB), that contains the majority of the known accreting X-ray pulsars with typical magnetic field strength equal or above $3 \times 10^{11} \text{ G}$

([Ikhsanov & Mereghetti 2015](#); [Christodoulou et al. 2016](#)). In BeXRBs material is provided by a non-supergiant Be type donor star. This is a young stellar object that rotates with a near-critical rotation velocity, resulting in strong mass loss via an equatorial decretion disk ([Krtićka et al. 2011](#)). As BeXRBs are composed of young objects, their number within a galaxy correlates with the recent star formation (e.g. [Antonioni et al. 2010](#); [Antonioni & Zezas 2016](#)). By monitoring BeXRB outbursts, it is now generally accepted that normal or so-called Type-I outbursts ($L_x \sim 10^{36} \text{ erg s}^{-1}$) can occur as the NS passes close to the decretion disk, thus they appear to be correlated with the binary orbital period. Giant or Type-II outbursts ($L_x \geq 10^{38} \text{ erg s}^{-1}$) that can last multiple orbits are associated with wrapped Be-disks ([Okazaki et al. 2013](#)). From an observational point of view the former can be quite regular, appearing in each orbit (e.g. LXP 38.55 & EXO 2030+375 [Vasilopoulos et al. 2016](#); [Wilson et al. 2008](#)) while for other systems they are more sparse ([Kuehnel et al. 2015](#)). On the other hand, major outbursts producing $10^{38} \text{ erg s}^{-1}$ are rare events with only a hand-full detected every year. Moreover, it is only during these events that the pulsating NS can reach super-Eddington luminosities, thus providing a link between accreting NS and the emerging population of NS-ULXs. ([Bachetti et al. 2014](#); [Fürst et al. 2016](#); [Israel et al. 2017a,b](#)).

The spectroscopic study of BeXRB outbursts in our Galaxy is hampered by the strong Galactic absorption, and the often large uncertainties in their distances. The Magellanic Clouds (MCs) offer a unique laboratory to study BeXRB outbursts. Their moderate and well measured distances of $\sim 50 \text{ kpc}$ for the Large Magellanic Cloud (LMC) ([Pietrzyński et al. 2013](#)) and $\sim 62 \text{ kpc}$ for the Small Magellanic Cloud (SMC) ([Graczyk et al. 2014](#)) as well as their low Galactic foreground absorption ($\sim 6 \times 10^{20} \text{ cm}^{-2}$) makes them ideal targets for this task.

The 2016 major outburst of SMC X-3 offers a rare opportunity to study accretion physics onto a highly magnetized NS during an episode of high mass accretion. SMC X-3 was one of the earliest X-ray systems to be discovered in the SMC in 1977 by the SAS 3 satellite at a luminosity level of about $10^{38} \text{ erg s}^{-1}$ ([Clark et al. 1978](#)). The pulsating nature of the system was revealed more than two decades later when 7.78 s pulsations were measured ([Corbet et al. 2003](#)) using data from the Proportional Counter Array on board the Rossi X-ray Timing Explorer (PCA, RXTE [Jahoda et al. 2006](#)), and a proper association was possible due to analysis of archival *Chandra* observations ([Edge et al. 2004](#)). By investigating the long term optical light-curve of the optical counterpart of SMC X-3, [Cowley & Schmidtke \(2004\)](#) reported a 44.86 d modulation that they interpreted as the orbital period of the system. [McBride et al. \(2008\)](#) have reported a spectral type of B1-1.5 IV-V for the BeXRB’s donor star.

The 2016 major outburst of SMC X-3 was first reported by MAXI ([Negoro et al. 2016](#)) and is estimated to have started around June 2016 ([Kennea et al. 2016](#)), while the system still remains active at the time of writing (June 2017). Lasting for more than seven binary orbital periods the 2016 outburst can be classified as one of the longest ever observed for any BeXRB system. Since the outburst was reported the system has been extensively monitored in the X-rays by *Swift* with short visits, while deeper observations have been performed by NuSTAR, *Chandra* and *XMM-Newton*. [Townsend et al. \(2017\)](#) have reported a 44.918 d period as the true orbital period of the system by modeling the pulsar period (see also [Weng et al. 2017](#)) evolution during the 2016 outburst with data obtained by *Swift*/XRT and by analyzing the optical light-curve of the system, obtained from the Optical Gravitational Lensing Experiment (OGLE, [Udalski et al. 2015](#)).

The maximum luminosity obtained by *Swift*/XRT imposes an above-average maximum magnetic field strength at the NS surface ($> 10^{13}$ G), as does the lack of any cyclotron resonance feature in the high energy X-ray spectrum of the system (Pottschmidt et al. 2016; Tsygankov et al. 2017). On the other hand, the lack of a transition to the propeller regime, during the evolution of the 2016 outburst suggests a much weaker magnetic field at the magnetospheric radius. According to Tsygankov et al. (2017) this apparent contradiction could be resolved if there was a significant non-bipolar component of the magnetic field close to the NS surface.

Following the evolution of the outburst we requested a non anticipated *XMM-Newton* ToO observation (PI: F. Koliopanos) in order to perform a detailed study of the soft X-ray spectral characteristics of the system. In § 2 we describe the spectral and temporal analysis of the *XMM-Newton* data. In § 3 we introduce a toy model constructed to phenomenologically explain our findings, and in § 4 and § 5 we discuss our findings and their interpretation, in the context of highly accreting X-ray pulsars in (or at the threshold of) the ultraluminous regime.

2. Observations and data analysis

2.1. *XMM-Newton* data extraction

XMM-Newton observed SMC X-3 on the 14th of October 2016 for a duration of ~ 37 ks. All on board instruments were operational, with MOS2 and pn operating in Timing Mode and MOS1 in Large Window Mode. All detectors had the Medium optical blocking filter on. In Timing mode data are registered in one dimension, along the column axis. This results in considerably shorter CCD readout time which increases spectral resolution but also protects observations of bright sources from pile-up¹.

Spectra from all detectors were extracted using the latest *XMM-Newton* Data Analysis software SAS, version 15.0.0. and using the calibration files released² on May 12, 2016. The observations were inspected for high background flaring activity, by extracting high energy light curves ($E > 10$ keV for MOS and $10 < E < 12$ keV for pn) with a 100 s bin size. The examination revealed ~ 2.5 ks of the pn data that were contaminated by high energy flares. The contaminated intervals were subsequently removed. The spectral extraction was done using SAS task `evselect`, with the standard filtering flags (`#XMEA_EP && PATTERN <= 4` for pn and `#XMEA_EM && PATTERN <= 12` for MOS). SAS tasks `rmfgen` and `arfgen` were used to create the redistribution matrix and ancillary file. MOS1 data were suffering from pile-up and for this reason they were rejected. For simplicity and self-consistency, we opted to only use the EPIC-pn data in our spectral analysis. The pn spectra are optimally calibrated for spectral fitting and had $\sim 1.3 \times 10^6$ registered counts, allowing to accurately constrain emission features and minute spectral variations between spectra extracted during different pulse phases. While, an official estimation is not provided by the *XMM-Newton* SOC the pn data, in timing mode, are expected to suffer from systematic uncertainties in the 1-2% range (e.g. see Appendix A in Díaz Trigo et al. 2014). Accordingly, we have quadratically added 1% systematic errors to each energy bin of the pn data. The spectra from the Reflection Grating Spectrometer (RGS, den Herder et al. 2001) were extracted using SAS task `rgsproc`. The resulting RGS1 and RG2 spectra were combined using `rgscombine`.

¹ For more information on pile-up see: <http://xmm2.esac.esa.int/docs/documents/CAL-TN-0050-1-0.ps.gz>

² *XMM-Newton* CCF Release Note: XMM-CCF-REL-334

2.2. *Swift* data extraction

To study the long-term behavior of the source hardness, pulse fraction and evolution throughout the 2016 outburst we also analyzed the available *Swift*/XRT data up to December 31st, 2016. The data were analyzed following the instructions described in the *Swift* data analysis guide³ (Evans et al. 2007). We used `xrtpipeline` to generate the *Swift*/XRT products, while events were extracted by using the command line interface `xselect` available through HEASoft FTOOLS (Blackburn 1995)⁴. Source events were extracted from a $45''$ region, while background was extracted from an annulus between $90''$ and $120''$.

2.3. X-ray timing analysis

We searched for a periodic signal in the barycentric corrected EPIC-pn event arrival time series by using an epoch folding technique (EF: Davies 1990; Larsson 1996). The EF method uses a series of trial periods within an appropriate range to phase fold the detected event arrival times and performs a χ^2 minimization test of a constant signal hypothesis. Folding a periodic light curve with an arbitrary period smears out the signal and the folded profile is expected to be nearly flat. Thus a large value of the χ^2 (i.e. a bad fit) indirectly supports the presence of a periodic signal. A disadvantage of this method is that it lacks proper determination of the period uncertainty. In many cases, the full width at half maximum of the χ^2 distribution is used as an estimate for the uncertainty, but this value only improves with the length of the time series and not with the number of events (Gregory & Loredo 1996) and does not have the meaning of the statistical uncertainty. In order to have a correct estimate for both the period and its error, we applied the Gregory-Loredo method of Bayesian Periodic Signal Detection (Gregory & Loredo 1996), and constrained the search around the true period derived from the epoch folding method. To further test the accuracy in the derived pulsed period we performed 100 repetitions of the above method while bootstrapping the event arrival times and by selecting different energy bands with 1.0 keV width (e.g. 2.0-3.0 keV, 3.0-4.0 keV). The derived period deviation between the above samples was never above 10^{-5} sec. From the above treatment we derived a best fit pulse period of 7.77200(6) s. The pulse profile corresponding to the best fit period is plotted in Fig. 1. The accurate calculation of the pulse profile enabled us to compute the pulsed fraction (PF), which is defined as the ratio between the difference and the sum of the maximum and minimum count rates over the pulse profile i.e.

$$PF = (F_{max} - F_{min}) / (F_{max} + F_{min}). \quad (1)$$

For the *XMM-Newton* EPIC-pn pulse profile (Fig. 1) we calculated a pulsed fraction of $PF = 0.328 \pm 0.005$. We also estimated the PF for five energy bands – henceforth noted with the letter i , with $i = 1, 2, 3, 4, 5$ and $1 \rightarrow (0.2 - 0.5)$ keV, $2 \rightarrow (0.5 - 1.0)$ keV, $3 \rightarrow (1.0 - 2.0)$ keV, $4 \rightarrow (2.0 - 4.5)$ keV, $5 \rightarrow (4.5 - 10.0)$ keV (Watson et al. 2009; Sturm et al. 2013). The resulting values for the energy-resolved PF are $PF_1 = 0.208$, $PF_2 = 0.249$, $PF_3 = 0.341$, $PF_4 = 0.402$, $PF_5 = 0.410$.

In Fig. 2 we present the phase-folded light curves for the five energy bands introduced above, together with the four phase-resolved hardness ratios. The hardness ratios HR_i ($i = 1, 2, 3, 4$) are defined as:

$$HR_i = \frac{R_{i+1} - R_i}{R_{i+1} + R_i} \quad (2)$$

³ <http://www.swift.ac.uk/analysis/xrt/>

⁴ <http://heasarc.gsfc.nasa.gov/ftools/>

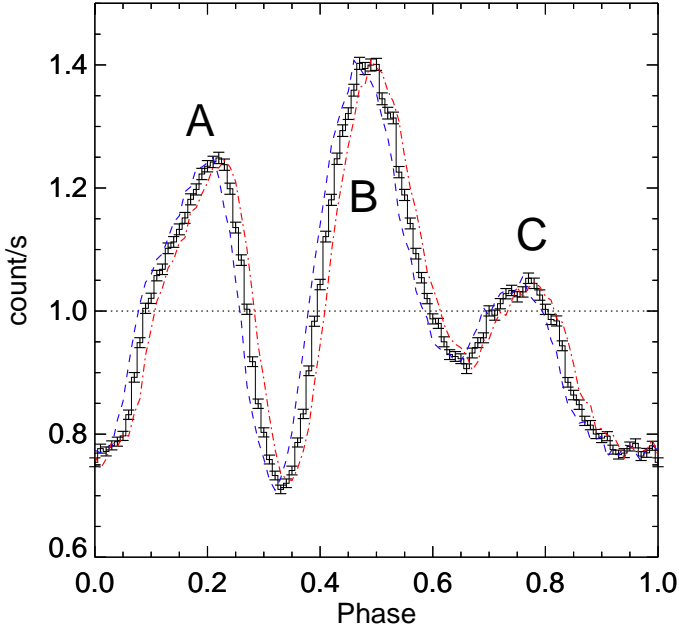


Fig. 1: Phase folded pulse profile of SMC X-3 derived from the best fit period of 7.7720059. Profile is normalized at an average count rate of 44.49 cts s⁻¹. Red and blue lines correspond to the derived pulse profile for a period shifted by $\pm 5 \times 10^{-5}$ s which is ~ 1000 times larger than the derived period uncertainty. This was chosen to demonstrate the accuracy of the derived period. Three peaks are clearly distinguished.

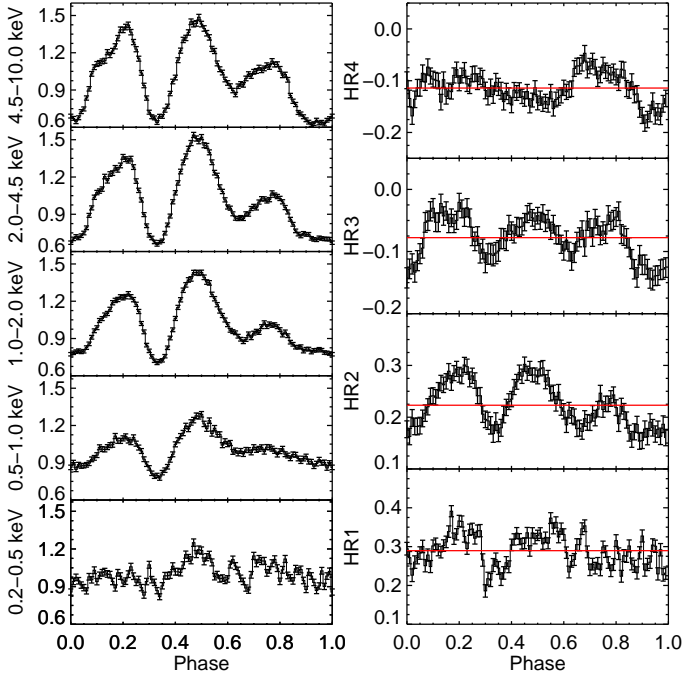


Fig. 2: *Left*: Pulse profiles of SMC X-3 obtained from the EPIC-pn data in different energy bands. The profiles are background subtracted and normalized to their average count rate (from bottom to top: 4.33, 7.90, 12.6, 10.9 and 8.68 cts s⁻¹). *Right*: Hardness ratios derived from the pulse profiles in two neighboring standard energy bands as a function of pulse phase. red horizontal lines denote the pulse-phase average HR.

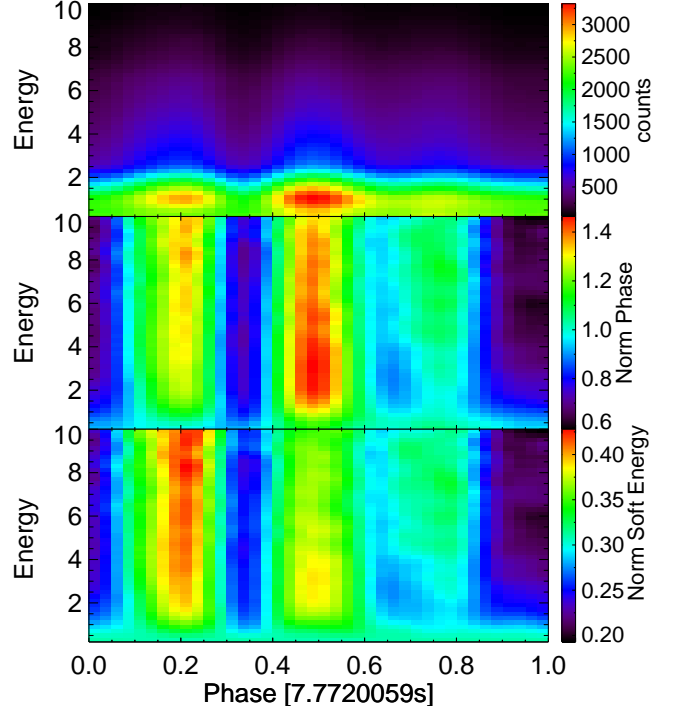


Fig. 3: Phase dependent spectral heat map, obtained by binning the EPIC-pn source counts to 40 phase and 50 energy bins. Top: Colors are proportional to the number of counts per bin. Middle: Data rates are corrected for the EPIC-pn response matrix efficiency and normalised by the phase-averaged number of counts in each energy bin. Bottom: Data normalised a second time using the rate average of each phase bin for the soft X-ray band (0.2-0.6 keV).

With R_i denoting the background-subtracted count rate in the i^{th} energy band. The plots revealed that the prominence of the three major peaks are strongly dependent on the energy range. Namely, the pulsed emission appears to be dominated by high energy (i.e. > 2 keV) photons, while in the softer bands the pulse shape is less pronounced. To better visualize the spectral dependence of the pulse phase we produced a 2D-histogram for the number of events as function of energy and phase (top panel of Fig. 3). The histogram of the events covers a large dynamic range due to the strongly varying efficiency of the camera and telescope with energy. To produce an image where patterns and features (such as the peak of the pulse) are more easily recognized we normalized the histogram by the detector's average effective area for the given energy bin and then we normalized it a second time by the phase-averaged count rate in each energy bin (middle panel, Fig. 3). Lastly, in the lower bin each phase-energy bin was divided by the average soft X-ray flux (0.2-0.6 keV) of the same phase bin (bottom panel, Fig. 3). This energy range was chosen because it displays minimum phase variability (Fig. 2).

2.4. X-ray spectral analysis

We performed phase averaged and phase resolved spectroscopy of the pn data and a separate analysis of the RGS data. Analysis was performed using the latest version of the XSPEC fitting package, Version 12.9.1 (Arnaud 1996). The spectral continuum – in both phase averaged and phased resolved spectroscopy – was modeled using a combination of an absorbed multi-

color disk black body (MCD) and a power-law component. The interstellar absorption was modeled using the `tbnew` code, which is a new and improved version of the X-ray absorption model `tbabs` (Wilms et al. 2011). The atomic cross sections were adopted from Verner et al. (1996). We considered a combination of Galactic foreground absorption and an additional column density accounting for both the interstellar medium of the SMC and the intrinsic absorption of the source. For the Galactic photo-electric absorption we considered a fixed column density of $nH_{\text{GAL}} = 7.06 \times 10^{20} \text{ cm}^2$ (Dickey & Lockman 1990), with abundances taken from Wilms et al. (2000).

2.4.1. Phase averaged spectroscopy

Both thermal and non-thermal emission components, were required to successfully fit the spectral continuum. More specifically, when modeling the continuum using a simple power law, there was a pronounced residual structure which strongly indicated the presence of thermal emission below 1 keV. On the other hand, non-thermal emission dominated the spectrum at higher energies. The thermal emission was modeled by a MCD model (for the rationale of this choice see discussion in Section 4), which we modeled using the XSPEC model `diskbb`. The continuum emission models alone could not fit the spectrum successfully, and strong emission-like residuals were noted at ~ 0.51 , ~ 0.97 and ~ 6.63 keV and yielded a reduced χ^2 value of 1.93 for 198 dof. (see ratio plot in Fig. 4). The corresponding emission features were modeled using gaussian curves, yielding a χ^2 value of 1.01 for 190 dof. The three emission lines are centered at $E_1 \sim 0.51$ keV, $E_2 \sim 0.96$ keV and $E_3 \sim 6.64$ keV and have equivalent width values of $6.6^{+5.0}_{-4.1}$ eV, $19^{+7.0}_{-5.1}$ eV and 72^{+17}_{-15} eV, respectively. The E_2 and E_3 lines have a width of $83.8^{+3.0}_{-2.6}$ eV and $361^{+89.7}_{-80.1}$ eV, respectively and the E_1 line was not resolved. The three emission-like features also appear in the two MOS detectors (see Fig. 4) and the RGS data. The presence of the emission like features in the MOS spectra increases the robustness of their detection, however the MOS data are not considered in this analysis. The MOS1 detector was heavily piled-up and since we use the pn detector for the phase-resolved spectroscopy (as it yields more than three times the number of counts of the MOS2 detector), we also opted to not consider the MOS2 data and only use the pn data for the phase-averaged spectroscopy, in order to maintain consistency. For display purposes we have plotted the MOS1, MOS2 and pn spectra and the data-to-model vs energy plots in Fig. 5. For the purposes of this plot we have fitted the spectra of the three detectors using the `diskbb` plus `powerlaw` model, with all their parameters left free to vary. This choice allows for the visual detection of the line-like features, while compensating for the considerable, artificial “hardening” of the piled-up MOS1 detector. The MOS data indicate that the line-like features at ~ 0.5 keV and ~ 1 keV are composed by more emission lines, that are unresolved by pn. This finding is confirmed by the RGS data (see section 2.4.3 for more details). Narrow residual features are still present in the 1.7–2.5 keV range. They, most likely stem from incorrect modeling of the Si and Au absorption in the CCD detectors, by the EPIC pn calibration, which often results in the presence of emission and/or absorption features at ~ 1.84 keV, ~ 2.28 keV ($M\beta$) and 2.4 keV ($M\gamma$). Since the features are not too pronounced and did not affect the quality of the fit or the values of the best fit parameters, they were ignored, but their respective energy channels were still included in our fits.

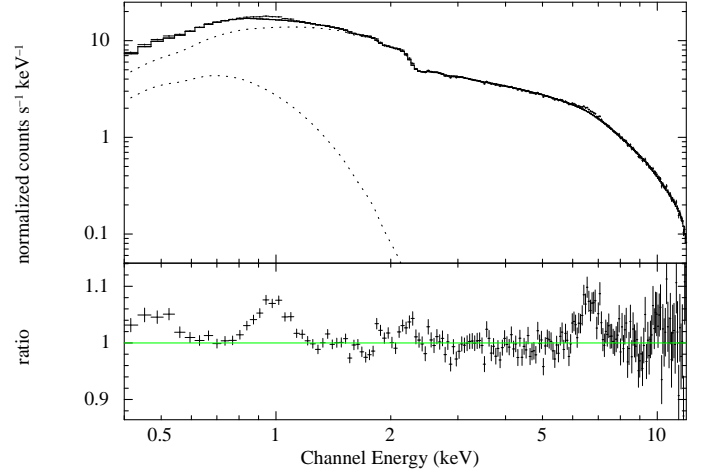


Fig. 4: Phase average X-ray spectrum, without the gaussian emission lines. *Top plot*: Normalized counts vs energy. *Bottom plot*: Data-to-model ratio plot.

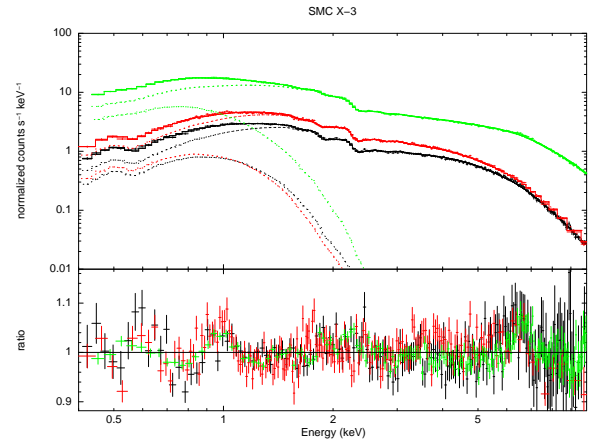


Fig. 5: Phase average X-ray spectrum, with only the continuum model for all EPIC detectors (black: MOS1, red: MOS2, green: pn). *Top plot*: Normalized counts vs energy. *Bottom plot*: Data-to-model ratio plot.

The best fit parameters for the modeling of the phase-averaged pn data are presented in Tables 1 and 2, with the normalization parameters of the two continuum components given in terms of their relevant fluxes (calculated using the multiplicative XSPEC model `cflux`). The phase averaged pn spectrum along with the data-to-model ratio plot (without the gaussian emission lines) is presented in Figure 4. The phase averaged spectrum was also modeled using a single temperature black body instead of the MCD component. The fit was qualitatively similar to the MCD fit, with a kT_{BB} temperature of 0.19 ± 0.01 keV, a size of $168^{+22.1}_{-16.4}$ km and a power-law spectral index of 0.98 ± 0.01 .

2.4.2. Phase resolved spectroscopy

We created separate spectra from twenty phase intervals of equal duration. We studied the resulting, phase resolved spectra by fitting each individual spectrum separately using the same model as in the phase-averaged spectrum. We noted the behavior of the

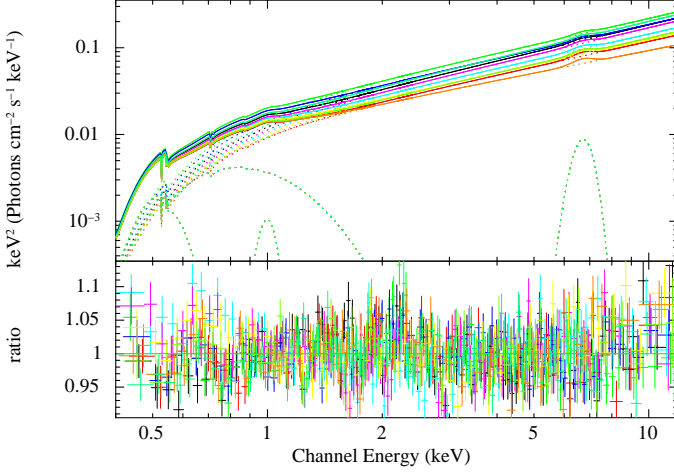


Fig. 6: Spectral model and data-to-ratio plot of the simultaneous fit of the twenty phase-resolved spectra

two spectral components and the three emission lines, and monitored the variation of their best fit parameters as the pulse phase evolved. The resulting best fit values for the continuum are presented in Table 1 and of the emission lines in Table 2. In Figure 7 we present the evolution of the different spectral parameters and the source count rate with the pulse phase.

For purposes of presentation and to further note the persistent nature of the soft emission, we also fit all twenty spectra simultaneously and tied the parameters of the thermal component, while the parameters of the power-law component were left free to vary. The results of this analysis were qualitatively similar to the independent spectral fitting (see Fig. 6 were the spectral evolution of the source is illustrated). Nevertheless the decision to freeze the temperature and normalization of the soft component at the phase-averaged best-fit value, introduces bias to our fit and for this reason we only tabulate and study the best-fit values for the independent modeling of the phase resolved spectra.

2.4.3. RGS spectroscopy

The RGS spectra were not grouped and were fitted employing Cash statistics (Cash 1979) and with the same continuum model as the phased averaged pn spectra. The model yielded an acceptable fit, with a reduced χ^2 value of 1.05 for 1875 dof. The RGS spectra were also fitted simultaneously with the pn phase-averaged spectra (with the addition of a normalization constant which was left free to vary) yielding best-fit parameter values consistent within 1σ error bars with the pn continuum model. We therefore froze the continuum parameters to the values tabulated in the first row of Table 1. We note that a simple absorbed power-law model still describes the continuum with sufficient accuracy, and the use of a second component only improves the fit by $\sim 2.7\sigma$ as indicated by performing an *ftest*⁵.

We searched the RGS spectra for emission and absorption lines by a blind search for gaussian features with a fixed width the spectrum was searched by adding the Gaussian to the continuum and fitting the spectrum, with a step of 10 eV and the resulting ΔC was estimated for each step. Emission and absorption lines detected with a more than 3σ significance. To estimate the

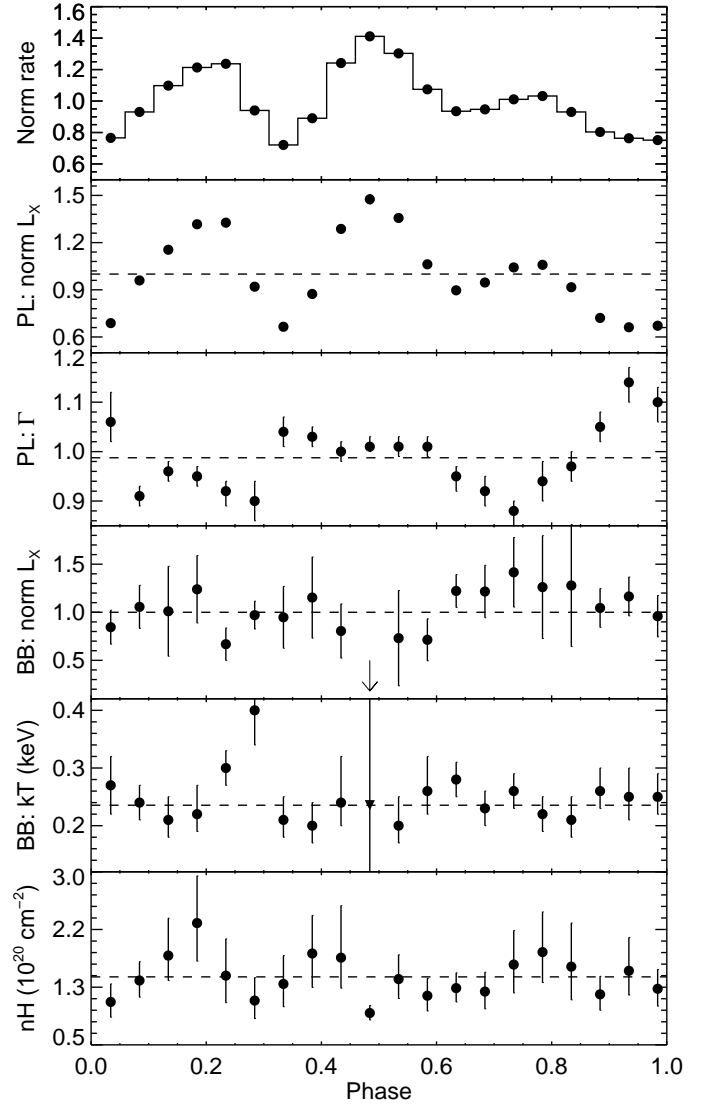


Fig. 7: Evolution of spectral parameters (Table 1) for the phase resolved spectroscopy presented in 2.4.2. The arrow symbol represent the upper limit for the flux of the MCD component on phase-resolved spectrum #5. The corresponding temperature was frozen to the phase-averaged value (see first row of Table 1).

values for the ΔC that correspond to the 3σ significance we followed a similar approach to Kosec et al. (2018). We simulated 1000 spectra based on the continuum model and repeated the process of line-search using the fixed width Gaussian the resulting ΔC values outside the 99.7% of the entire sample correspond to $\Delta C \approx 6$. In Fig. 8 we have plotted the ΔC improvement of emission and absorption lines detected in the RGS data assuming Gaussian lines with a fixed width of 2 eV (black solid line) and 10 eV (orange dashed line). The line significance is affected by the width of the gaussian and a more thorough approach should include a grid of different line widths in order to achieve the best fit. For this work we noted the emission lines with more than 3σ significance (dotted line) assuming a 2 eV fixed width, which were then fitted “manually” with the width as a free parameter, the best fit values are presented in table 3. We also note the presence of a strong absorption line at more than 5σ significance and several tentative others. The most prominent absorption line centered at ≈ 1.585 keV, if the line is associated with MgXII ab-

⁵ Algorithms taken from CEPHES special function library, by Stephen; Moshier. (<http://www.netlib.org/cephes/>)

sorption it appears to be blue-shifted by 7%. The apparent blue-shift could be an indication of outflows, but the velocity appears to be considerable lower than the velocities inferred for ULXs (e.g. Pinto et al. 2016). A more thorough study of the RGS data, using an extended grid of all line parameters will be part of a separate publication.

2.5. X-ray spectral and temporal evolution during the 2016 outburst

We report on the longterm evolution of the values of the PF and HR throughout the 2016 outburst, using the data from *Swift* observatory. Using the method described in §2.3 we searched for the pulse period of SMC X-3 for all the analyzed *Swift*/XRT observations using the barycentric corrected events within the 0.5–10.0 keV energy band. The resulted pulse periods are presented in Fig. 9. Using the derived best fit periods we estimate the PF for all the *Swift*/XRT observations (see Fig. 10). From the extracted event files we calculated the phase average hardness ratios for all *Swift*/XRT observations. For simplicity and in order to increase statistics we used three energy bands to estimate two HR values. HR *soft* using the 0.5–2.0 keV and 2.0–4.5 keV bands, and HR *hard* using the 2.0–4.5 keV and 4.5–10.0 keV bands.

We performed the same calculations for the phase resolved spectrum of SMC X-3 as measured by the *XMM-Newton* ToO. In particular we estimated the above two HR values for 40 phase intervals. The evolution of the spectral state of SMC X-3 with time and pulse phase as depicted by these two HR values is shown in Fig. 11 (left). For comparison we have plotted in parallel (Fig. 11-right) the evolution of the HR with NS spin phase during the *XMM-Newton* observation. We note that although quantitatively different HR values are expected for different instruments (i.e. *Swift*/XRT and *XMM-Newton*/EPIC-pn), a qualitative comparison of the HR evolution can be drawn. More specifically, the left-hand plot probes the longterm HR evolution versus the mass accretion rate (inferred from the registered source count-rate), and the right-hand side the HR evolution with pulse phase.

3. Emission pattern, pulse reprocessing and the observed PF

To investigate the evolution of the PF with luminosity and to investigate the origin of the soft excess as determined from the phase resolved analysis, we constructed a toy-model for the beamed emission. The model assumes that the primary, beamed emission of the accretion column is emitted perpendicularly to the magnetic field axis, in a “fan beam” pattern (Basko & Sunyaev 1976). Furthermore, it is assumed that all the emission originates in a point source at a height of $\sim 2 - 3$ km from the surface of the NS. A fraction of the “fan” emission will also be beamed towards the NS surface, off of which it will be reflected, resulting in a secondary “polar” beam that is directed perpendicularly to the fan beam (this setup is described in Trümper et al. 2013, see also their Fig. 4). Partial beaming of the primary fan emission towards the NS surface is expected to occur primarily due to scattering by fast electrons at the edge of accretion column (Kaminker et al. 1976; Lyubarskii & Syunyaev 1988; Poutanen et al. 2013), and to a lesser degree due to gravitational bending of the fan-beam emission. The latter may also result in the emission of the far-away pole entering the observer line-of-sight. In the model, gravitational bending is accounted for, following the predictions of Beloborodov (2002).

The size of the accretion column (and hence the height of the origin of the fan-beam emission) is a function of the NS surface magnetic field strength and the mass accretion rate (see Mushtukov et al. 2015, and references within). As it changes, it will affect the size of the illuminated region on the NS surface and therefore the strength of the reflected “polar” emission. If the accretion rate drops below the critical limit, the accretion column becomes optically thin in the direction parallel to the magnetic field axis, and the primary emission is then described by the pencil beam pattern Basko & Sunyaev (1975). In principle the polar and pencil beam emission patterns can be phenomenologically described by the same algebraic model. We also model the irradiation of any slab or structure (e.g. the inner part of the accretion disk, that is located close to the NS), by the combined beams. Lastly, while arc-like accretion columns and hot-spots have been found in 3D magnetohydrodynamic simulations (Romanova et al. 2004) of accreting pulsars, we did not include them in our treatment as they would merely introduce an anisotropy in the pulse profile and not significantly affect our results.

3.1. Pulsed fraction evolution

The beaming functions of the polar and fan beams are given by $f \sin^m \phi$ and $p \cos^k \phi$, respectively. Here ϕ is the angle between the magnetic field axis and the photon propagation, and is thus a function of the angle between the magnetic and rotation axis (θ), the angle of the NS rotation axis the observing angle (i) and the NS spin phase. The exponent values m and k can be as low as one, but in the general case of the accretion column emission they can have significantly larger values (Trümper et al. 2013). We constructed various pulse profiles for different combinations of fan and polar beam emission patterns with different relative intensities of the fan and polar beams (i.e. $F_{\text{Polar}}/F_{\text{Fan}}$ ranging from ~ 0.01 to ~ 30). We note that these values exceed any realistic configuration between the fan beam and the reflected polar beam. More specifically, since the polar beam is a result of reflection of the fan beam, it is only for very limited range of observing angles that its contribution will (seemingly) exceed that of the fan beam, and thus a value of $F_{\text{Polar}}/F_{\text{Fan}} \gtrsim 2$, is unlikely. On the other hand, the increasing height of the emitting region – which would result in a smaller fraction of the fan beam being reflected by the NS surface – is limited to $\lesssim 10$ km (Mushtukov et al. 2015), thus limiting the $F_{\text{Polar}}/F_{\text{Fan}}$ ratio to values greater than 0.1 (see e.g. fig 2. of Poutanen et al. 2013). Despite these physical limitations we have extended our estimations to these exaggerated values in order to better illustrate the contribution of each component (fan and polar) to the PF. Moreover, a value of $F_{\text{Polar}}/F_{\text{Fan}}$ exceeding 10 qualitatively describes the pencil-beam regime, which is expected at lower accretion rates. We estimated the PF for a range of observer angles and for different combinations of angles between the magnetic and rotation axis. An indicative result for a 45° angle between the NS magnetic field and rotation axis and for an $r_G/r_{\text{NS}} = 0.25$ is plotted in Fig 12.

3.2. Reprocessed radiation

To investigate the origin of the soft excess (i.e. the thermal component in the spectral fits) and to assess its contribution to the pulsed emission, we studied the pattern of the reprocessed emission from irradiated, optically thick material in the vicinity of the magnetosphere. More specifically we consider a cylindrical re-

Table 1: Best fit parameters for the continuum for the 20 phases and the phase-averaged spectrum. All errors are in the 90% confidence range.

Phase	$nH^{[a]}$	kT_{soft}	$F_{\text{soft}}^{[b]}$	Γ	$F_{\text{PO}}^{[c]}$	count-rate	χ^2/dof
	$[\times 10^{21} \text{ cm}^2]$	keV	$10^{-11} \text{ erg cm}^{-2} \text{ s}^{-1}$		$10^{-11} \text{ erg cm}^{-2} \text{ s}^{-1}$	cts/s	
Average	$1.36^{+0.13}_{-0.62}$	$0.24^{+0.04}_{-0.03}$	1.44 ± 0.19	0.98 ± 0.10	29.8 ± 0.95	41.8 ± 0.04	1.01/190
0	$1.50^{+0.53}_{-0.39}$	0.30 ± 0.03	1.17 ± 0.30	$0.92^{+0.02}_{-0.03}$	40.1 ± 0.37	52.5 ± 0.19	1.05/181
1	$1.14^{+0.35}_{-0.26}$	$0.40^{+0.07}_{-0.06}$	1.70 ± 0.25	0.90 ± 0.04	27.8 ± 0.29	39.9 ± 0.17	0.95/177
2	$1.38^{+0.41}_{-0.33}$	$0.21^{+0.04}_{-0.03}$	1.66 ± 0.60	1.04 ± 0.03	20.1 ± 0.25	30.6 ± 0.17	1.01/169
3	$1.82^{+0.55}_{-0.49}$	$0.20^{+0.04}_{-0.03}$	2.02 ± 0.74	1.03 ± 0.02	26.4 ± 0.28	37.8 ± 0.17	1.03/171
4	$1.76^{+0.45}_{-0.44}$	$0.24^{+0.08}_{-0.04}$	1.41 ± 0.50	1.00 ± 0.02	38.9 ± 0.35	52.7 ± 0.21	1.00/183
5	$0.96^{+0.11}_{-0.10}$	—	< 2.17	1.01 ± 0.01	44.6 ± 0.90	59.9 ± 0.20	0.87/184
6	$1.45^{+0.35}_{-0.28}$	$0.20^{+0.05}_{-0.03}$	1.28 ± 0.87	1.01 ± 0.02	41.0 ± 0.35	55.3 ± 0.19	1.01/187
7	$1.21^{+0.25}_{-0.22}$	$0.26^{+0.06}_{-0.04}$	1.25 ± 0.38	1.01 ± 0.02	32.1 ± 0.37	45.6 ± 0.20	0.89/182
8	$1.32^{+0.22}_{-0.20}$	0.28 ± 0.03	2.14 ± 0.30	0.95 ± 0.03	27.1 ± 0.34	39.7 ± 0.17	0.81/178
9	$1.27^{+0.28}_{-0.25}$	0.23 ± 0.03	2.13 ± 0.48	0.92 ± 0.03	28.6 ± 0.40	40.2 ± 0.17	0.88/178
10	$1.66^{+0.49}_{-0.41}$	0.26 ± 0.03	2.48 ± 0.63	$0.88^{+0.02}_{-0.03}$	31.5 ± 0.28	42.9 ± 0.18	0.87/182
11	$1.84^{+0.58}_{-0.44}$	0.22 ± 0.03	2.21 ± 0.94	0.94 ± 0.04	32.0 ± 0.46	43.8 ± 0.18	1.08/178
12	$1.63^{+0.63}_{-0.48}$	$0.21^{+0.04}_{-0.03}$	2.24 ± 1.11	0.97 ± 0.03	27.7 ± 0.37	39.5 ± 0.17	1.09/173
13	$1.23^{+0.26}_{-0.23}$	$0.26^{+0.03}_{-0.03}$	1.83 ± 0.35	1.05 ± 0.03	21.8 ± 0.26	34.1 ± 0.17	0.99/173
14	$1.57^{+0.48}_{-0.38}$	$0.25^{+0.05}_{-0.04}$	2.04 ± 0.35	$1.14^{+0.03}_{-0.04}$	20.0 ± 0.25	32.4 ± 0.15	0.89/170
15	$1.31^{+0.28}_{-0.25}$	$0.25^{+0.04}_{-0.03}$	1.68 ± 0.38	$1.10^{+0.03}_{-0.04}$	20.3 ± 0.25	31.9 ± 0.15	1.07/170
16	$1.12^{+0.26}_{-0.22}$	0.27 ± 0.05	0.15 ± 0.31	$1.06^{+0.06}_{-0.04}$	20.9 ± 0.26	32.5 ± 0.15	1.01/172
17	$1.43^{+0.27}_{-0.24}$	0.24 ± 0.03	1.85 ± 0.39	0.91 ± 0.02	29.0 ± 0.31	39.5 ± 0.17	0.94/187
18	$1.79^{+0.54}_{-0.36}$	$0.21^{+0.04}_{-0.03}$	1.77 ± 0.82	0.96 ± 0.02	34.9 ± 0.33	46.6 ± 0.18	1.11/178
19	$2.26^{+0.68}_{-0.55}$	$0.22^{+0.05}_{-0.03}$	2.17 ± 0.61	0.95 ± 0.02	39.8 ± 0.36	51.5 ± 0.19	0.96/182

Notes. ^(a) Column density of the intrinsic absorption. The galactic foreground absorption was fixed to a value of . The Galactic column density was fixed to $nH_{\text{GAL}} = 7.06 \times 10^{20} \text{ cm}^2$ (Dickey & Lockman 1990), with abundances taken from Wilms et al. (2000).

^(b) Unabsorbed “Bolometric” X-ray flux of the BB in the 0.2–12 keV band

^(c) Unabsorbed X-ray flux in the 0.2–12 keV band. For the distance of 62 kpc (Graczyk et al. 2014), a conversion factor of $4.6 \times 10^{47} \text{ cm}^{-2}$ can be used to convert from flux to luminosity.

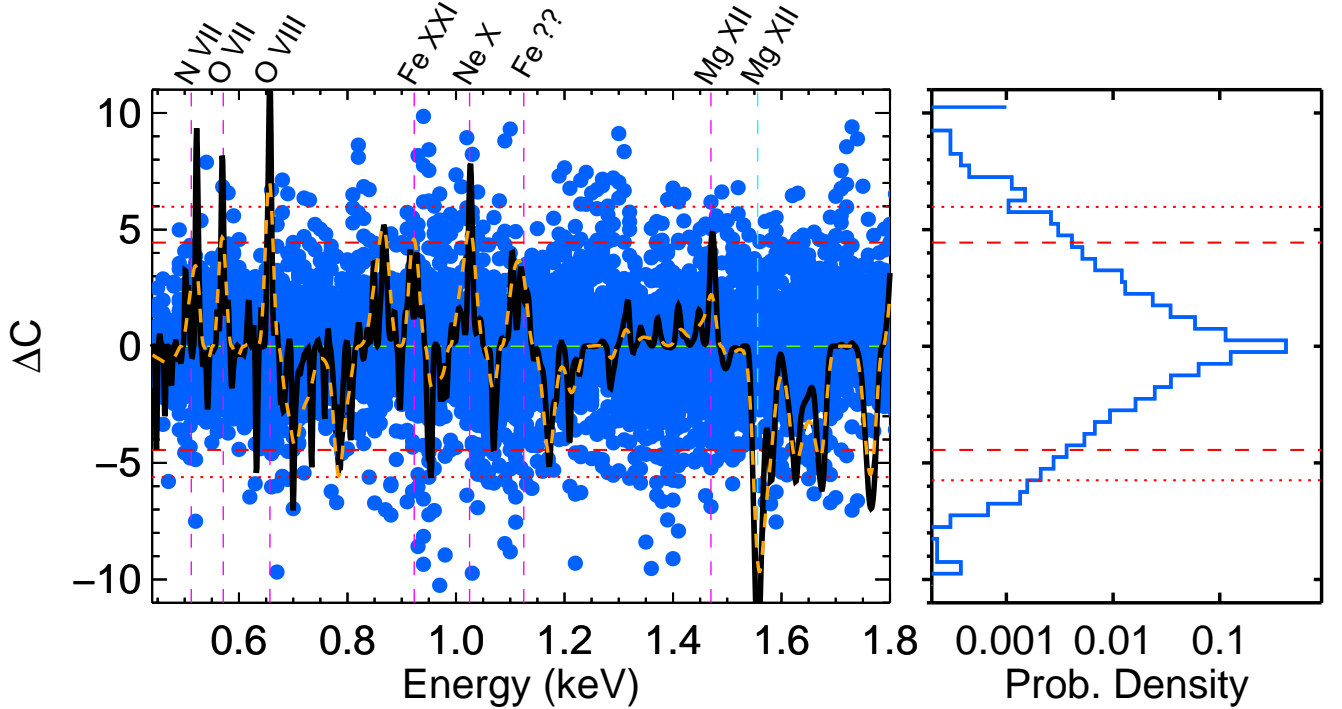


Fig. 8: Emission and absorption lines detected in the RGS data. *Left plot:* ΔC for each line vs energy. Black color corresponds to gaussians with 2 eV width and orange to 10 eV width. The blue points correspond to the simulated spectra of the model continuum. *Right plot:* Probability density function for ΔC values for the simulated spectra. Dashed line corresponds to three standard deviations assuming that the prob. density function follows the gaussian distribution. Dotted line: encloses 99.7% of the ΔC values.

Table 2: Best fit parameters for the emission lines for the 20 phases. All errors are in the 90% confidence range.

Phase	E ₁	K ₁	E ₂	K ₃	E ₃	σ_3	K ₃
	keV	10 ⁻⁴ cts cm ⁻² s ⁻¹	keV	10 ⁻⁴ cts cm ⁻² s ⁻¹	keV	keV	10 ⁻⁴ cts cm ⁻² s ⁻¹
Average ^a	0.51±0.02	3.02 ^{+2.36} _{-1.78}	0.96±0.02	3.55 ^{+1.32} _{-0.98}	6.64 ^{+0.16} _{-0.15}	0.36 ^{+0.09} _{-0.08}	1.70 ^{+0.39} _{-0.35}
0	0.49±0.03	11.2 ^{+15.8} _{-8.52}	0.98±0.03	2.79 ^{+1.18} _{-1.19}	6.76 ^{+0.16} _{-0.15}	0.25 ^{+0.20} _{-0.15}	2.43 ^{+1.40} _{-1.23}
1	0.51 ^{+0.04} _{-0.03}	6.98 ^{+8.06} _{-5.27}	0.94 ^{+0.06} _{-0.05}	1.91±1.13	6.44 ^{+0.20} _{-0.32}	< 0.39	1.33 ^{+0.96} _{-0.82}
2	0.53 ^{+0.09} _{-0.15}	<10.8	1.02 ^{+0.02} _{-0.03}	2.69 ^{+0.97} _{-0.89}	6.76 ^{+0.26} _{-0.30}	0.45*	2.28 ^{+1.10} _{-1.15}
3	0.50 ^{+0.06} _{-0.05}	<21.9	0.97±0.03	2.75 ^{+1.19} _{-1.16}	6.49 ^{+0.14} _{-0.26}	< 0.48	0.92 ^{+1.13} _{-0.62}
4	0.48 ^{+0.03} _{-0.02}	16.8 ^{+23.5} _{-12.5}	—	—	—	—	—
5	0.55 ^{+0.08} _{-0.04}	4.96 ^{+5.21} _{-4.31}	0.98±0.03	3.12±1.13	6.61 ^{+0.26} _{-0.30}	0.41 ^{+0.34} _{-0.22}	3.06 ^{+2.08} _{-1.53}
6	—	—	—	—	—	—	—
7	—	—	0.94±0.03	2.69±1.23	—	—	—
8	—	—	—	—	6.74 ^{+0.22} _{-0.24}	0.28 ^{+0.38} _{-0.24}	1.80 ^{+1.54} _{-1.07}
9	—	—	0.98 ^{+0.03} _{-0.02}	3.09 ^{+1.10} _{-1.08}	6.81 ^{+0.31} _{-0.28}	0.45*	2.93±1.13
10	0.46±0.04	16.0 ^{+21.9} _{-13.1}	—	—	—	—	—
11	0.50 ^{+0.03} _{-0.02}	14.7 ^{+20.2} _{-10.6}	0.94±0.03	3.12±1.17	6.76 ^{+0.29} _{-0.39}	0.45*	2.97 ^{+1.29} _{-1.30}
12	0.46 ^{+0.03} _{-0.04}	<8.90	0.97±0.03	2.30 ^{+1.14} _{-1.13}	6.70 ^{+0.20} _{-0.19}	0.45*	3.60 ^{+1.25} _{-1.41}
13	—	—	0.96 ^{+0.05} _{-0.09}	1.70 ^{+1.06} _{-1.07}	—	—	—
14	0.51 ^{+0.08} _{-0.05}	7.49 ^{+14.1} _{-6.58}	0.99 ^{+0.03} _{-0.04}	1.85 ^{+1.04} _{-1.03}	6.9*	0.44 ^{+0.20} _{-0.16}	2.52 ^{+1.25} _{-1.14}
15	—	—	0.95 ^{+0.16} _{-0.07}	1.13 ^{+1.06} _{-1.04}	6.87 ^{+0.19} _{-0.12}	0.30 ^{+0.22} _{-0.12}	2.32 ^{+1.04} _{-0.93}
16	—	—	1.02 ^{+0.04} _{-0.08}	1.76 ^{+0.94} _{-0.93}	6.42 ^{+0.42} _{-0.19}	0.30 ^{+0.39} _{-0.14}	1.79 ^{+1.30} _{-0.90}
17	—	—	—	—	6.58 ^{+0.12} _{-0.11}	< 0.29	1.67 ^{+0.90} _{-0.87}
18	0.53±0.03	6.41 ^{+5.44} _{-5.31}	1.00 ^{+0.03} _{-0.04}	2.25 ^{+1.12} _{-1.17}	6.45±0.06	< 0.14	1.06±0.53
19	0.49±0.02	24.2 ^{+29.6} _{-16.0}	—	—	6.60 ^{+0.13} _{-0.36}	< 0.60	1.38 ^{+1.88} _{-0.91}

Notes. ^(a) The widths of lines E₁ and E₂ were frozen to the value of 1 eV in the phased resolved analysis. This was because they are too narrow to be resolved by the pn detector. Nevertheless E₂ in the face averaged spectra is broader and has a width value of $\sigma = 83.8^{+3.04}_{-2.56}$ eV.

Table 3: RGS emission lines and the corresponding the ΔC value for each added gaussian. All errors are in the 90% confidence range.

Line ^a	E	σ	norm	ΔC
eV	keV	eV	10 ⁻⁴ cts cm ⁻² s ⁻¹	
N VII (500.3)	0.512 ^{+0.011} _{-0.014}	16.02 ^{+13.00} _{-6.44}	3.152 ^{+1.510} _{-1.509}	12.5
O VII (561-574)	0.571±0.005	< 10.01	1.341 ^{+0.309} _{-0.893}	7.29
O VIII (653.6)	0.657 ^{+0.003} _{-0.03}	< 7.0	0.6 ^{+0.5} _{-0.3}	14.9
Fe XIX-XXI (917.2)	0.923±0.006	10.40 ^{+6.73} _{-3.39}	0.964 ^{+0.377} _{-0.371}	20.3
Ne X (1022)	1.025 ^{+0.003} _{-0.002}	3.481 ^{+15.09} _{-2.017}	0.653 ^{+0.247} _{-0.246}	20.6
Fe XXIII-XXIV (1125)	1.125 ^{+0.018} _{-0.020}	16.77 ^{+24.61} _{-11.55}	0.597±0.413	5.8

Notes. ^(a) Most likely emission lines assuming collisionally-ionized diffuse gas at a temperature of ~ 1 keV.

processing region, that extends symmetrically above and below the equatorial plane. The radius of the cylinder is taken to be equal to the magnetospheric radius, where the accretion disk is interrupted. The latitudinal size of the reprocessing region corresponds to an angular size of 10°, as viewed from the center of the accretor (see e.g. [Hickox et al. 2004](#), and our Fig. 16 for an illustration). The model takes into account irradiation of this region, by the combined polar- and fan-beam emission. If \mathbf{d} is the unit vector towards the observer and \mathbf{n} is the disc surface normal, the total radiative flux that the observer sees would be estimated from their angle $\mathbf{d} \cdot \mathbf{n}$. We further assume that the observer sees only half of the reprocessing region (and disk, i.e. π). Light travel effects of the scattered/reprocessed radiation (e.g. equation 3 of [Vasilopoulos & Petropoulou 2016](#)) should have a

negligible effect in altering the phase of the reprocessed emission, as the light crossing time of the disk is less than 1% (0.05% = $(1000\text{km}/c)/P_{\text{NS}} * 100\%$) of the NS spin period. Thus, any time lag that is expected should be similar in timescale to the reverberation lag observed in LMXB systems (e.g. H1743-322: [De Marco & Ponti 2016](#)).

To determine the fraction of the pulsed emission that illuminates the reprocessing region, we integrate the emission over the 10° angular size of the reprocessing region and estimate the PF for an inclination angle between the rotational and the magnetic filed axes (θ) that ranges between 0° and 90° (Fig. 13, dotted line). We also estimate the PF originating from the reprocessing region assuming a ratio of $F_{\text{Polar}}/F_{\text{Fan}} = 0.25$ (Fig. 13, solid line). To further probe the contribution of the two beam components to the reprocessed emission, we estimate the PF for two extreme cases in which all the primary emission is emitted in the polar⁶ beam (Fig. 13, green dashed line) or only the fan beam (Fig. 13, blue dashed line).

4. Discussion

The high quality of the *XMM-Newton* spectrum of SMC-X3 and the very large number of total registered counts, have allowed us to perform a detailed, time resolved spectroscopy where we robustly constrain the different emission components and monitor their evolution with pulse-phase. Furthermore, the high time resolution of the *XMM-Newton* detectors, complimented with the numerous Swift/XRT observations (conducted throughout the

⁶ As already discussed, this scenario is unrealistic, since the polar beam is the result of reflection of the fan beam. However this setup would adequately describe the “pencil” beam emission, expected at lower accretion rates (e.g. [Basko & Sunyaev 1975](#))

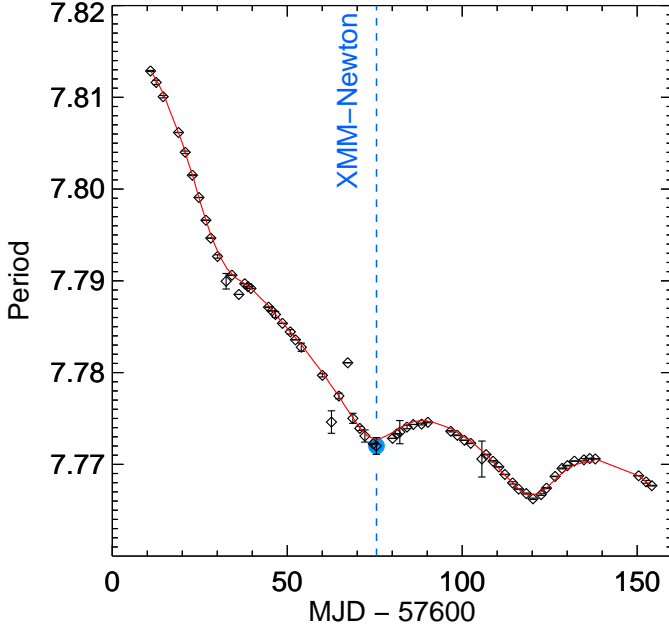


Fig. 9: Pulse period evolution during the 2016 burst of SMC X-3 based on the analysis of *Swift*/XRT data. Red line is based on the best fit model describing the evolution of the spin (Townsend et al. 2017). The date of the *XMM-Newton* pointing is marked by the blue-dashed vertical line. The spin period derived by the EPIC-pn data is marked with a blue circle, this solution coincides with the one derived from *Swift*/XRT on an observation performed within the same day.

outburst), have allowed for a detailed study of the long- and short-term temporal behavior of the source. Below, we present our findings and their implications with regard to the underlying

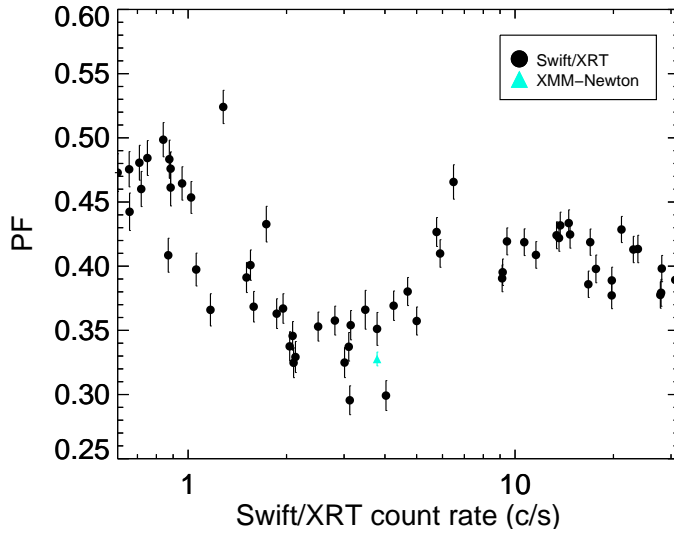


Fig. 10: PF: Pulsed fraction defined in equation 1. *Swift* errors are computed based on the poisson uncertainty of the pulse profile, and do not include calculations based on the period uncertainties, as systematic uncertainty of 0.01 was added to the estimated *Swift*/XRT PF. *XMM-Newton* PF is estimated from the profile presented in Fig. 1 and errors are estimated from the 1σ error in the derived period.

physical mechanisms, responsible for the observed characteristics.

4.1. The emission pattern of the accretion column and its evolution

The 0.01-12 keV luminosity of SMC X-3 during the *XMM-Newton* observation is estimated at $1.45 \pm 0.01 \times 10^{38}$ erg/s for a distance of ~ 62 kpc. The corresponding mass accretion rate, assuming an efficiency of $\xi = 0.21$ (e.g. Sibgatullin & Sunyaev 2000), is $\dot{M} \sim 1.2 \times 10^{-8} M_{\odot}/\text{yr}$, which places the source well within the fan-beam regime (Basko & Sunyaev 1976; Nagel 1981). Furthermore, the shape of the pulse profile (Fig. 1), indicates a more complex emission pattern, comprised of the primary fan beam and a secondary, reflected polar beam as was proposed in Trümper et al. (2013) and briefly presented in Section 3. The energy resolved pulse profiles and the phase resolved hardness ratios presented in Fig. 2 strongly indicate that the pulsed emission is dominated by hard-energy photons, while the smooth single-color appearance of the 0.2-0.6 keV energy range in the lower bin heat map presented in Fig. 3 indicates the presence of a soft spectral component that is not pulsating.

Using our toy-model for the emission of the accretion column, we were able to explore the evolution of the PF with the $F_{\text{Polar}}/F_{\text{Fan}}$ ratio, assuming a broad range of observer viewing angles. Interestingly the resulting PF vs $F_{\text{Polar}}/F_{\text{Fan}}$ ratio (Fig. 12), qualitatively resembles the evolution of the PF, with increasing source count-rate, as presented in Fig. 10, using *Swift*/XRT data. Following the paradigm of Basko & Sunyaev (1975) and Basko & Sunyaev (1976) we expect the emission pattern of the accretion column to shift from a pencil to a fan-beam pattern as accretion rate increases. Namely, below ~ 1 cts/sec the emission is dominated by the pencil beam (which is qualitatively similar to the polar beam). This regime is defined by $F_{\text{Polar}}/F_{\text{Fan}} > 2$. As the luminosity increases⁷, the radiation of the accretion column starts to be emitted in a fan beam, which is accompanied by the secondary polar beam, corresponding to $0.7 \leq F_{\text{Polar}}/F_{\text{Fan}} \leq 2$. This is the era during which the *XMM-Newton* observation was conducted. As accretion rate continued to increase, the accretion column grew larger, the height of emitting region increased and the emission started to become dominated by the fan-beam, as the reflected component decreases, yielding a smaller value of the $F_{\text{Polar}}/F_{\text{Fan}}$ ratio. Nevertheless, in Fig. 10 it is evident that the PF does not readily increase, as the fan beam becomes more predominant (i.e. above ~ 7 cts/s). This indicates that the height of the accretion column is limited to moderate values (e.g., as argued by Poutanen et al. 2013; Mushtukov et al. 2015) and therefore a considerable contribution from the polar beam is always present.

The presence of the polar beam is also indicated by the shape of the pulse profile and its evolution during different energy bands and HR values (Figures 1 and 2). The pulse profile features three distinct peaks, which we label “A”, “B” and “C”, from left to right in Fig. 1. The energy and HR-resolved pulse profiles presented in Fig. 2, reveal that the pulse peaks are dominated by harder emission. A closer inspection, indicates that peak B is “softer” than the other two peaks, and is still present (albeit much less pronounced) in the lower energy bands (Fig. 2, lower left bin). This finding is further supported by our study of the HR evolution of the sources throughout the *XMM-Newton* observa-

⁷ This only refers to the X-axis of Fig. 10 and does not imply chronological order. The chronological evolution is indicated with arrows in Fig. 11

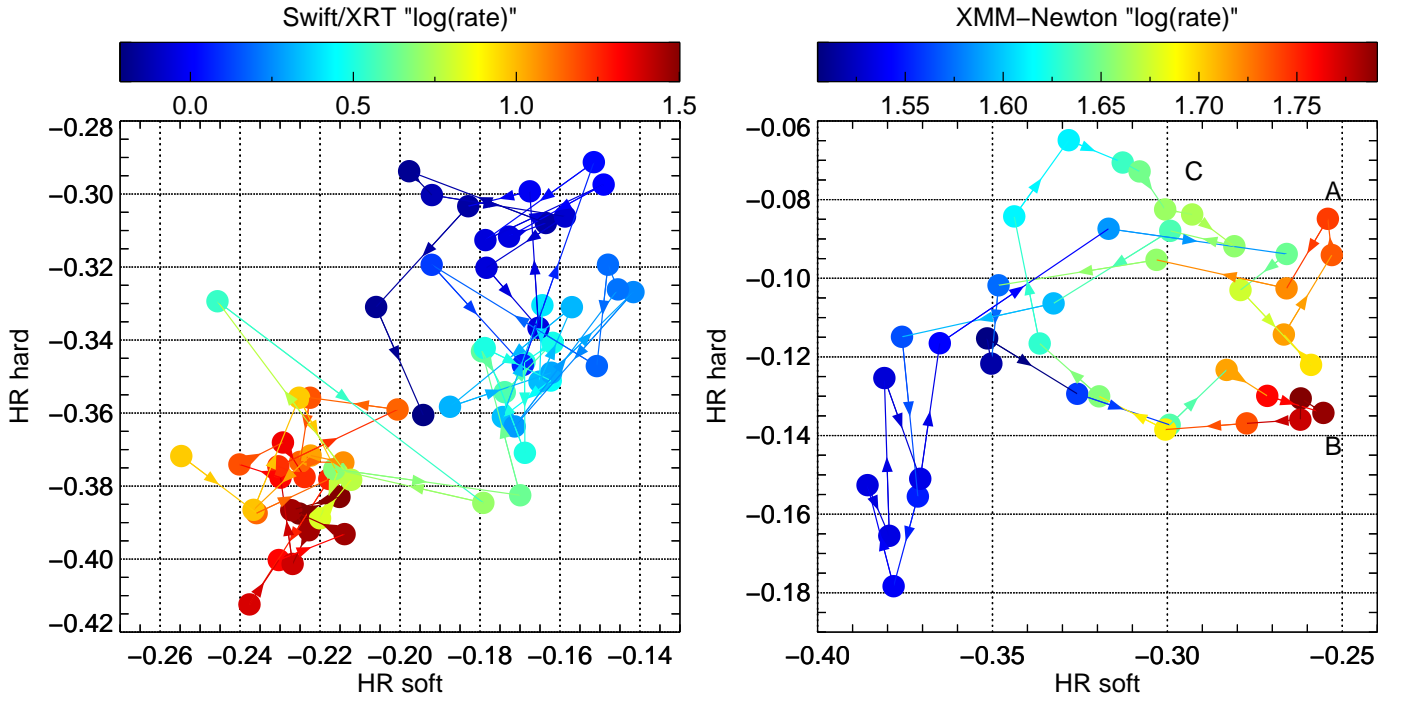


Fig. 11: *Left*: Hardness ratio evolution of the average X-ray spectrum of SMC X-3 as estimated for all *Swift*/XRT observations. Calculations were made using three bands 0.5-2.0 keV, 2.0-4.5 keV and 4.5-10.0 keV. HR soft was estimated using the 2 former energy bands, while HR hard was estimated for the later two. Colors are representative of the average count rate of each observation, while arrows connect observations in a chronological order. *Right*: Hardness ratio evolution of the phase resolved X-ray spectrum of SMC X-3 based on the *XMM-Newton* observation. HR were defined as in the left plot, while 40 phase bins were used. Colors are representative of the average count rate of each phase bin, while arrows connect observations based on their phase evolution. Labels “A”, “B” and “C” represent the three peaks in Fig. 1

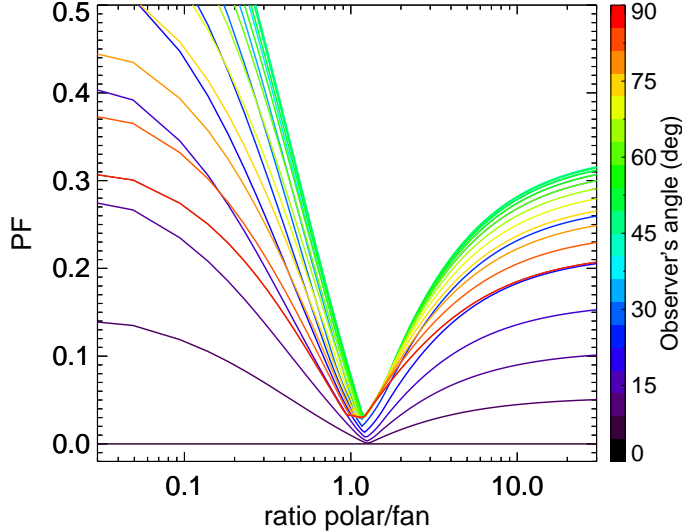


Fig. 12: PF versus intensity between fan and pencil beam.

tion, presented in Fig. 11 (right panel). In this representation, it is clearly demonstrated that the source is harder during high flux intervals (namely the peaks of the pulse profile), but also that peak B is distinctly softer than peaks A and C. We argue that these findings indicate a different origin of the three peaks. More specifically, we surmise that the softer and more prominent peak B originates mostly from the fan beam, while the two harder peaks (A,C) are dominated by the polar beam emission, which is expected to be harder than the fan beam. This is because only

the harder incident photons (of the fan beam) will be “reflected” (i.e. backscattered) off the NS atmosphere, while the softer ones will be absorbed (e.g. Trümper et al. 2013; Postnov et al. 2015).

The analysis of the *Swift* data taken throughout the outburst allowed us to also probe the long-term spectral evolution of the source. In the left panel of Fig. 11 we present the HR ratio evolution of the source throughout the 2016 outburst. Unlike the short term evolution of the source – during which, the emission is harder during the high-flux peaks of the pulses (see the data from the *XMM-Newton* observation presented in the right panel of Fig. 11) – in the long term the emission of SMC X-3 becomes softer, as the luminosity of the source increases (color-coded count rate in Fig. 11). This behavior is also evident in Fig. 15 where the HR ratio of the 1-3 keV to the 3-10 keV band is plotted versus the source count-rate. The source becomes clearly softer as the accretion rate (that corresponds to the observed flux) increases. Long-term observations of numerous XRP suggests that they can be divided into two groups, based on their long-term spectral variability. Sources in group 1 (e.g. 4U 0115+63) exhibit a positive correlation between source hardness and its flux, while sources in group 2 (e.g. Her X-1 or this source) a negative (e.g. Tsygankov et al. 2007, 2010; Vasco et al. 2011; Klochkov et al. 2011).

It can be argued that the apparent two populations are just the result of observing the XRPs in two different mass accretion rate regimes. At low accretion rates deceleration of the in-falling particles in the accretion column happens primarily via Coulomb interactions, while in the high-rate regime the mass is decelerated due to pressure from the strong radiation field (e.g. Basko & Sunyaev 1976; Wang & Frank 1981; Mushtukov et al.

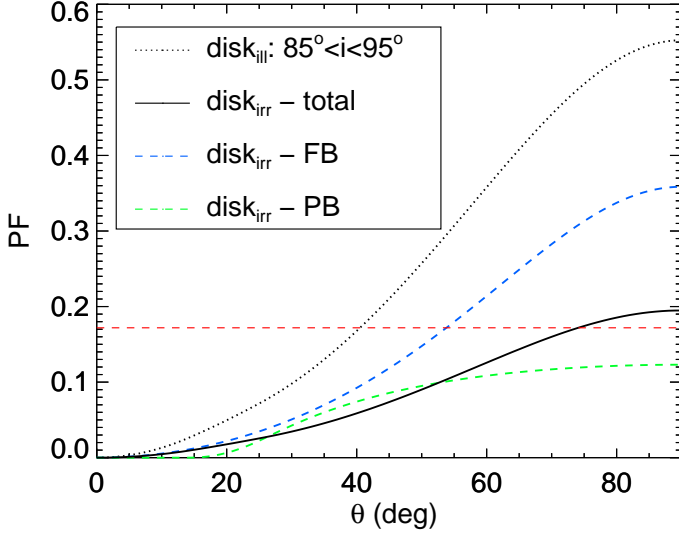


Fig. 13: PF of the reprocessed emission of a fan-beam pattern for various inclination angles between the magnetic and rotation axis. Dotted line represent the PF of the integrated emission over a cylindrical surface of angular size of 10° and located at the equatorial plane of the NS. Solid line is the calculated reprocessed PF for a combination of polar and fan beam ($F_{\text{Polar}}/F_{\text{Fan}} = 0.25$). Dashed blue and green lines show the PF of reprocessed emission that would originate from a pure fan-beam and polar-beam illuminating pattern, respectively. The red horizontal line represents the limit on the PF given the variability as of the observed flux of the thermal component, presented in Figure 7.

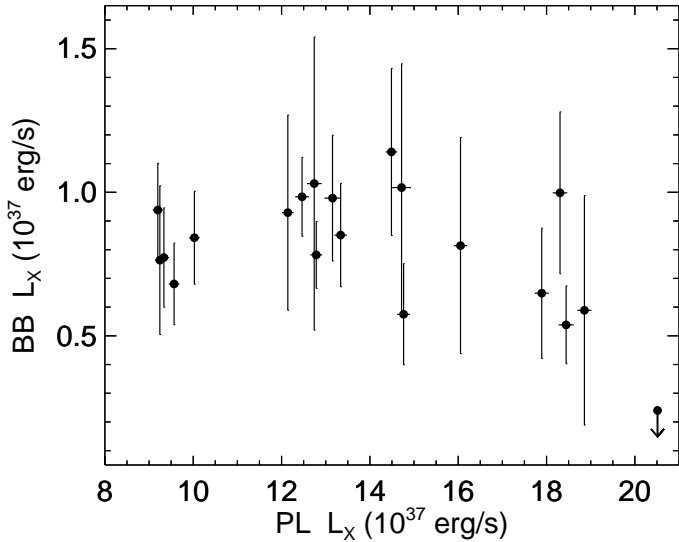


Fig. 14: Absorption corrected PL X-ray luminosity versus bolometric disk-BB luminosity. No clear correlation between the two quantities was established.

2015). As mass accretion rate increases, so does the height of the accretion column, and therefore the reflected fraction (i.e the polar beam) starts to decrease. As the polar emission is harder than the fan beam, the total registered spectrum stops hardening and even becomes moderately softer (Postnov et al. 2015). Observationally, the positive correlation is expected at luminosities below a critical value and the negative above it. This criti-

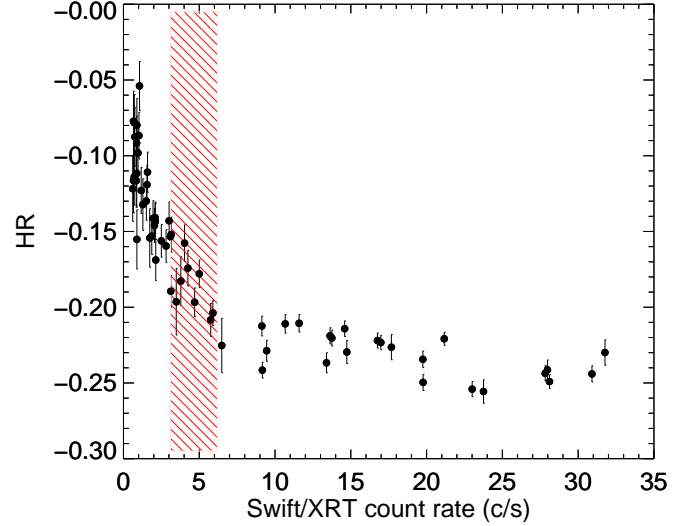


Fig. 15: Hardness ratio of the 1-3 keV to 3-10 keV bands versus count rate for the *Swift* observations of SMC X-3 between MJDs 57611 and 57754. The red-striped area denotes the luminosity corresponding to 1-2 Eddington rates (0.3-10 keV).

cal value is theoretically predicted at $\sim 1 - 7 \times 10^{37}$ erg/s (e.g. Staubert et al. 2007; Klochkov et al. 2011; Becker et al. 2012; Postnov et al. 2015), which is in agreement with the earlier prediction of Basko & Sunyaev (1976). Indeed, observations of XRP, at different luminosities, show that a single source can exhibit the behavior of both groups when monitored above or below this critical value (e.g. Postnov et al. 2015).

The high luminosity regime – which is the only regime probed by the *Swift* data points in Fig. 15 – is essentially the “diagonal” branch of the hardness-intensity diagrams presented in the paper of Reig & Nespoli (2013). The source behavior, presented in Fig. 15, is consistent with the theoretical predictions for sources accreting above the critical luminosity of $\sim 10^{37}$ erg/s. However, while the previous observations by Klochkov et al. (2011) and Postnov et al. (2015) show the pause in the hardening of the source with increasing luminosity, and – in some sources – the slight decrease in hardness, in this work this drop is clearly demonstrated, thanks to the numerous high quality observations provided by the *Swift* telescope. Furthermore, our analysis hints at the presence of perhaps a third branch – appearing when the source luminosity exceeds $\sim 4 \times L_{\text{Edd}}$ – in which the source luminosity increases but the emission does not become softer. If this additional branch is indeed real, it may have eluded detection in the Reig & Nespoli paper, simply because the sources studied there never reached such high luminosities. It is plausible that the stabilization of the source hardness is a manifestation of the predicted physical limitations imposed to the maximum height of the accretion column (e.g. Poutanen et al. 2013; Mushtukov et al. 2015).

4.2. The origin of the soft excess and the optically thin emission

The phase-averaged spectral continuum of SMC X-3 during the *XMM-Newton* observation is described by a combination of a hard power-law shaped emission and a softer thermal-component, with a temperature of ~ 0.24 keV. The non-thermal component is consistent with emission from the accretion col-

umn (e.g. Becker & Wolff 2007), but the origin of the soft thermal emission is less clear. Assuming that the accretion disk is truncated approximately at the magnetosphere, and for an estimated magnetic field of $\sim 2 - 3 \times 10^{12}$ G (Klus et al. 2014; Tsygankov et al. 2017), the maximum effective temperature of the accretion disk would lie in the far UV-range (20–30 eV), for $\dot{M} \sim 1.2 \times 10^{-8} M_{\odot}/\text{yr}$, as inferred from the observed luminosity and for $R_{\text{in}} = 0.5 - 1 R_{\text{mag}}$. Although we can exclude a typical thin disk as the origin of the emission, an inflated disk that is irradiated from the NS can be the origin of the thermal emission, as such a disk can reach higher temperatures (see e.g. Chashkina et al. 2017, and discussion below).

The emission is also unlikely to originate in hot plasma on the surface of the NS, as the size of a black body emitting sphere – that successfully fits the data – is an order of magnitude larger (~ 170 km) than the ~ 12 km radius of a $1.4 M_{\odot}$ NS. The observed thermal emission could be the result of reprocessing of the primary emission by optically thick material that lies at a distance from the NS and is large enough to partially cover the primary emitting region (i.e. the accretion column). If a significant fraction of the primary emission is reprocessed, then this optically thick region will emit thermal radiation at the observed temperatures. A detailed description of this configuration is presented in Endo et al. (2000) and Hickox et al. (2004). This optically thick material is composed of accreted material trapped inside the magnetosphere and also the inside edge of the accretion disk which at these accretion rates will start to become radiation dominated and geometrically thick (e.g. Shakura & Sunyaev 1973; Suleimanov et al. 2007; Chashkina et al. 2017). The reprocessing region, is expected to have a latitudinal temperature gradient and its emission can be modeled as a multi-temperature black body (e.g. Mushtukov et al. 2017), which we modeled using the XSPEC model `diskbb`. Nevertheless, we stress that the soft emission – most likely – does not originate in an accretion disk heated through viscous dissipation, but is rather the result of illumination of an optically thick region at the disk-magnetosphere boundary. Following Hickox et al. and assuming that the reprocessing region, subtends a solid angle Ω (as viewed from the source of the primary emission) has a luminosity given by $L_{\text{soft}} = (\Omega/4\pi) L_X$, where L_X is the observed luminosity and further assuming that the reprocessed emission is emitted isotropically and follows a thermal distribution (i.e. $L_{\text{soft}} = \Omega R^2 \sigma T_{\text{soft}}^4$), we can estimate the distance between the primary emitting region and the reprocessing region from the relation $R^2 = L_X / (4\pi \sigma T_{\text{soft}}^4)$ (Hickox et al. 2004).

For our best fit parameters and for a spectral hardening factor of $\sim 1.5 - 1.7$ (Shimura & Takahara 1995) the relation yields a value of $1.5 \pm 0.3 \times 10^8$ cm, which is in very good agreement with the estimated magnetospheric radius of $R_m = 1.6 \pm 0.4 \times 10^8$ cm, that corresponds to the expected (i.e. $\sim 2 - 3 \times 10^{12}$ G) magnetic field strength of SMC X-3 and for $R_m \sim 2 \times 10^7 \alpha \dot{M}_{15}^{-2/7} B_9^{4/7} M_{1.4}^{-1/7} R_6^{12/7}$ cm (Ghosh et al. 1977; Ghosh & Lamb 1979a,b, 1992), where α is a constant that depends on the geometry of the accretion flow with $\alpha=0.5$ being the commonly used value for disk accretion, \dot{M}_{15} is the mass accretion rate in units of 10^{15} g/s (estimated for the observed luminosity of $\sim 1.5 \times 10^{38}$ erg/s and assuming efficiency of 0.2), B_9 is the NS magnetic field in units of 10^9 G, $M_{1.4}$ is the NS mass in units of 1.4 times the solar mass and R_6 is the NS radius in units of 10^6 cm.

Three prominent, broad emission lines are featured on top of the broadband continuum. Centered at ~ 0.51 keV ~ 0.97 keV and ~ 6.64 keV, the lines are consistent with emission from hot, ionized plasma. The 6.6 keV line is most likely due to K-shell

fluorescence from highly ionized iron, while the 0.5 keV line is most likely the $K\alpha$ line of the N VII - Ly α (500) ion. The 1 keV line is most likely the combined result of Ne $K\alpha$ and Fe L-shell emission lines. Both the 1 keV and 6.6 keV lines appear to be broadened, although as we discuss below the broadening is most likely artificial. The result of blending of unresolved emission lines from relevant atoms at different ionization states. Both the 1 keV and the 6.6 keV lines are often detected in the spectra of XRBs and appear to be particularly pronounced in the spectra of X-ray pulsars (e.g. Boirin & Parmar 2003; Díaz Trigo et al. 2006; Ng et al. 2010; Kolehmainen et al. 2014). While, in many XRBs the emission lines (and particularly the iron $K\alpha$ line), are attributed to “reflection” of the primary emission from the optically thick accretion disk (e.g. Gilfanov 2010, and references therein), in the case of X-ray pulsars (and in this source), the emission line origin is more consistent with optically thin emission from rarefied hot plasma, trapped in the Alfvén shell of the highly magnetized NS (e.g. Basko 1978). Namely, the (apparent) line broadening is consistent with microscopic processes – i.e. Compton scatterings for a scattering optical depth of 0.5–1 (e.g. equation 30 in Basko 1978) – rather than macroscopic motions, such as the rotation of the accretion disk or the surface of the donor star. Indeed the measured width of the two lines correspond to line of sight velocities of $\sim 1.6 \times 10^4$ km/sec. For the disk inclination of $\lesssim 45^\circ$, expected for SMC X-3 (Townsend et al. 2017), this corresponds to a 3D velocity of $\gtrsim 2.3 \times 10^4$ km/sec. Assuming Keplerian rotation these velocities would correspond to a distance of $\lesssim 350$ km from the NS, which is almost an order of magnitude smaller than the estimated magnetospheric radius. Furthermore, the phase resolved pn spectra and the RGS spectra (discussed below) indicate that the line broadening may be an artifact, resulting from the blending of unresolved thin emission lines at different centroid energies.

4.3. Short-term evolution of the spectral continuum and emission lines.

The timing analysis of the source emission has revealed that the pulsed emission is dominated by hard photons (Fig. 3), furthermore the phase-folded light-curves reveal the presence of a non-pulsating component of the total emission, at energies below ~ 1 keV (see Fig. 2 and Fig. 3, bottom). The soft, persistent component of the source light curve, appears to coincide with the thermal spectral component. To investigate this further, we divided the pn spectra into twenty equally timed phase intervals, which were modeled independently. We find that, while the contribution from the soft thermal component is – more or less – stable (Fig. 14), the contribution of the power law component, strongly correlates with the pulse profile (Fig. 7). We note, though, that the use of a simple power law, in our spectral fittings, fails to model the low energy roll-over expected from a photon distribution which is the result of multiple Compton up-scatterings of soft, thermal seed photons. Nevertheless, adding an extra parameter for the low-energy turn-over would only add to the uncertainties of the soft component parameters, but would not qualitatively affect these findings. The variation of the power-law component is also illustrated in Fig. 6, in which the phase resolved spectra were unfolded from the phase averaged model. This behavior further supports the presence of a large, optically thick reprocessing region located at a considerable distance (i.e. the magnetospheric boundary). As demonstrated in Fig. 13, the reprocessed emission contributes a very small fraction of the pulsed emission.

This finding contradicts the conclusions of [Manousakis et al. \(2009\)](#) regarding another known Be-XRB, XMMU J054134.7-682550. In their work [Manousakis et al.](#) also note the presence of thermal emission in the spectrum of the source (they simultaneously analyze *XMM-Newton* and RXTE data) which they also attribute to reprocessing of the primary emission by optically thick material. However, contrary to this work, [Manousakis et al.](#) conclude that the reprocessed emission is also pulsating. They further argue that this is the result of highly beamed emission from the pulsar emitted towards the inner disk border. The authors reach this conclusion by noticing the (tentative) presence of a sinusoidal-like shape of the pulse profile in the $\lesssim 1$ keV range. They then conclude that this is mostly due to the contribution of the reprocessed emission. However, the seeming pulsations of the soft component may be due to the fact that [Manousakis et al.](#) do not distinguish between the 0.5-1 keV and <0.5 keV energy range, as the total number of counts in their observation did not allow it. It is highly likely that the authors were probing the lower energy part of the accretion column emission, rather than the reprocessed, thermal emission. Indeed in our Fig. 2 (left) peaks “B” (and to a lesser extent “A”) are still detected in the 0.5-1 keV range and it is only below ~ 0.5 keV (where the thermal component dominates the emission) that the pulses disappear. More importantly, the high quality of our observation, allowed us to perform the detailed pulse-resolved analysis that demonstrated the invariance of the thermal component.

Furthermore, the fan-beam emission is not expected to be extremely narrow and – while optically thick material in the disk/magnetosphere boundary are expected to become illuminated by the primary emission (as both this work and [Manousakis et al. 2009](#) propose) – there is no reason to expect that the beam will be preferentially (and entirely) aimed towards the disk inner edge (especially when one accounts for the gravitational bending). Of course XMMU J054134.7-682550 could be a special case in which such an arrangement took place. However, we conclude that, most likely, the higher quality of the data available for SMC X-3 allowed for a more detailed analysis that revealed the non-pulsating nature of the thermal emission. This finding highlights the importance of long exposure, high resolution observations of X-ray pulsars.

The emission lines noted in the phase-averaged spectra are also detected in (most of) the phase resolved spectra. Their apparent strength and centroid energy variation between different phases (when the lines are detected, see table 2) lies within the 90% confidence range. However, the lines completely disappear during some phase intervals. While there is no discerning pattern between the presence (or absence) of the lines and the pulse phase, this variability is striking. Furthermore, it is strongly indicated (from the RGS data) that the seemingly broadened lines of the phase-averaged pn spectrum are the result of blending of narrow emission features at different centroid energies. The presence and variability of multiple emission lines indicates the presence of optically thin material that is located close to the central source and has a complex shape. As the different parts of this structure are illuminated by the central source, their ionization state varies with phase and position, resulting in emission lines with moderately different energies and different strengths. Such a complex structure is also supported by the predictions of ([Romanova et al. 2004](#)) for accretion of hot plasma onto highly magnetized NSs.

Based on our line identification – in the RGS data – no significant blue-shift can be established for the emission lines listed in Table 3. We note that similar lines have been reported in the X-ray spectra of other BeXRBs during outbursts (e.g. SMC X-

2, SXP 2.16 [La Palombara et al. 2016](#); [Vasilopoulos et al. 2017](#)). For SMC X-2 that was observed by *XMM-Newton* during a luminosity of $\sim 1.4 \times 10^{38}$ erg s $^{-1}$ (0.3-12.0 keV band) it has been proposed that these lines could be associated with the circum-source photo-ionized material in the reprocessing region at the inner disk ([La Palombara et al. 2016](#)). However, if the apparent emission line variability noted in our analysis is real, this would indicate a complex structure of optically thin plasma that lies closer to the source of the primary emission and is illuminated by it at different time intervals. Photoionized material at the boundary of the magnetosphere would not exhibit such rapid variability.

4.4. SMC X-3 in the context of ULX pulsars

It is interesting to note that all the emission lines resolved in SMC X-3 have been also identified in ultraluminous X-ray sources (NGC1313X-1 and NGC5408X-1, [Pinto et al. 2016, 2017b](#)) and ultraluminous soft X-ray sources (NGC 55 ULX, [Pinto et al. 2017a](#)). Moreover, there are striking similarities between the 1 keV emission feature of SMC X-3 and the same feature as described for NGC 55 ULX within the above studies; “emission peak at 1 keV and absorption-like features on both sides” ([Pinto et al. 2017a](#)). However we note that for SMC X-3 and other BeXRB systems (to our best knowledge) no significant blue-shift of the above mentioned lines has been measured. That could mean that these lines are produced by the same mechanism both in BeXRB systems (observed at luminosities around the Eddington limit) and in ULXs. However, in BeXRBs there is no ultrafast wind/outflow as in the case of ULX systems.

The findings of this work, regarding the continuum and line emission and their temporal variations, construct a picture of X-ray pulsars in which the accretion disk is truncated at a large distance from the NS (i.e. the magnetosphere), after which accretion is governed by the magnetic field. As material is trapped by the magnetic field, an optically thick structure is formed inside the pulsar magnetosphere, which (for a range of viewing angles) covers the primary source, partially reprocessing its radiation. The optically thick region is expected to have an angular size of the order of a \sim a few tens of degrees and to be centered at the latitudinal position of the accretion disk. At higher latitudes and closer to the accretion column, the trapped plasma, remains optically thin, producing the observed emission lines. This configuration is schematically represented in Fig. 16 and is in agreement with similar schemes proposed by [Endo et al. \(2000\)](#) and [Hickox et al. \(2004\)](#). At high accretion rates, the size of the reprocessing region becomes large enough to reprocess a measurable fraction of the primary emission. This is due to the increase in the accreting material trapped by the pulsar magnetosphere and the increase in the thickness of the accretion disk due to the increase of the radiation pressure (e.g. [Shakura & Sunyaev 1973](#); [Poutanen et al. 2007](#); [Dotan & Shaviv 2011](#); [Chashkina et al. 2017](#)).

This optically thick reprocessing region has been noted in numerous X-ray pulsars (e.g. Cen X-3: [Burderi et al. 2000](#); Her X-1: [Ramsay et al. 2002](#); LXP 8.04: [Vasilopoulos et al. in prep](#); SMC X-1: [Hickox & Vrtillek 2005](#); SMC X-2: [La Palombara et al. 2016](#)). Its presence in sub- or moderately super-Eddington accreting sources, becomes especially pertinent in light of recent publications where it is postulated, that at even higher accretion rates (corresponding to luminosities exceeding 10^{39} erg/s, i.e. in the ULX regime), the entire magnetosphere becomes dominated by optically thick material, which reprocesses all the primary photons of the accretion column

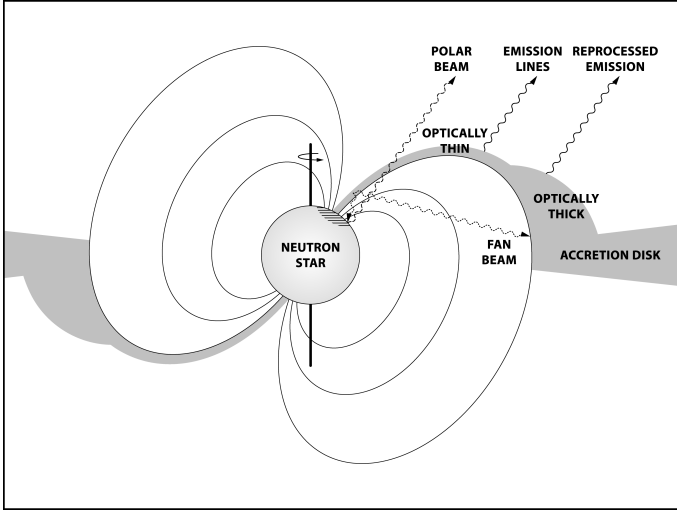


Fig. 16: A schematic representation of the proposed structural configuration of X-ray pulsars at the moderately high accretion regime. The (possibly inflated) accretion disk is truncated at approximately the magnetosphere and a combination of optically thick and thin plasma, is trapped at the magnetospheric boundary. The optically thick material (and the inner disk edge) partially cover the primary emission source and reprocess its emission. At higher latitudes the material remains optically thin. This is the origin of the emission lines. The source of the primary emission is located at a some height above the NS pole, inside the accretion column. We stress that the drawing is only aimed to better illustrate the discussed configuration and does not attempt to realistically reproduce the geometry of an accreting highly magnetised NS. More specifically, for viewing clarity, the emission pattern and direction of the fan and polar beams has been oversimplified and the inner disk radius (and size of the magnetosphere) has been greatly depreciated (e.g. in a more realistic example both components may illuminate the reprocessing region). The regions where the optically thin and thick plasma are expected to lie, have also been presented in a very simplified, minimalist arrangement.

(Mushtukov et al. 2017), essentially “washing out” the pulsation information and the spectral characteristics of the accretion column emission. The prediction of this model, have further been used to argue that a considerable fraction ULXs may in fact be accreting, highly magnetized NSs, rather than black holes (Koliopanos et al. 2017). In light of these considerations, SMC X-3 is of particular significance, since it stands right at the threshold between sub-Eddington X-ray pulsars and ULXs, and its spectro-temporal characteristics support the notion of a reprocessing region that is already of considerable size.

5. Conclusion

We have analyzed, the high quality *XMM-Newton* observation of SMC X-3, during its recent outburst. The *XMM-Newton* data where complimented with *Swift*/XRT observations, which were used to study the logn-term behavior of the source. By carrying out a detailed temporal and spectral analysis (including phase resolved spectroscopy) of the source emission, we find that its behavior and temporal and spectral characteristics adhere to the theoretical expectations and the previously noted observational traits of accreting highly magnetised NSs at high accretion rates. More specifically, we find indications of a complex emission pat-

tern of the primary, pulsed radiation, which most likely involves a combination of a “fan” beam emission component directed perpendicularly to the magnetic field axis and a secondary “polar” beam component reflected off the NS surface and directed perpendicularly to the primary, fan beam (as discussed in e.g. Basko & Sunyaev 1976; Wang & Frank 1981 and more recently Trümper et al. 2013).

The spectroscopic analysis of the source, further reveals the presence of optically thick material located at approximately the boundary of the magnetosphere. The reprocessing region has an angular size (as viewed from the NS), that is large enough to reprocess a considerable fraction of the primary, beamed emission which is remitted in the form of a soft thermal-like component that contributes very little to the pulsed emission. These findings are in agreement with previous works on X-ray pulsars (e.g. Endo et al. 2000; Hickox et al. 2004), but also the theoretical predictions for highly super-Eddington accretion onto highly magnetized NSs (e.g. King et al. 2017; Mushtukov et al. 2017; Koliopanos et al. 2017), where it is argued that this reprocessing region grows to the point that it may reprocess the entire pulsar emission.

6. Acknowledgements

The authors thank Maria Petropoulou for valuable advice and stimulating discussion. The authors also extend their warm gratitude to Cheryl Woynarski and woyadesign.com, for designing the source schematic. Finally we extend our gratitude to the anonymous referee, whose keen observations significantly improved our manuscript.

References

- Antoniou, V. & Zezas, A. 2016, MNRAS, 459, 528
- Antoniou, V., Zezas, A., Hatzidimitriou, D., & Kalogera, V. 2010, ApJ, 716, L140
- Arnaud, K. A. 1996, in Astronomical Society of the Pacific Conference Series, Vol. 101, Astronomical Data Analysis Software and Systems V, ed. G. H. Jacoby & J. Barnes, 17
- Bachetti, M., Harrison, F. A., Walton, D. J., et al. 2014, Nature, 514, 202
- Basko, M. M. 1978, ApJ, 223, 268
- Basko, M. M. 1980, A&A, 87, 330
- Basko, M. M. & Sunyaev, R. A. 1975, A&A, 42, 311
- Basko, M. M. & Sunyaev, R. A. 1976, MNRAS, 175, 395
- Becker, P. A., Klochkov, D., Schönherr, G., et al. 2012, A&A, 544, A123
- Becker, P. A. & Wolff, M. T. 2007, ApJ, 654, 435
- Beloborodov, A. M. 2002, ApJ, 566, L85
- Blackburn, J. K. 1995, in Astronomical Society of the Pacific Conference Series, Vol. 77, Astronomical Data Analysis Software and Systems IV, ed. R. A. Shaw, H. E. Payne, & J. J. E. Hayes, 367
- Borin, L. & Parmar, A. N. 2003, A&A, 407, 1079
- Burderi, L., Di Salvo, T., Robba, N. R., La Barbera, A., & Guainazzi, M. 2000, ApJ, 530, 429
- Burnard, D. J., Arons, J., & Klein, R. I. 1991, ApJ, 367, 575
- Caballero, I. & Wilms, J. 2012, Mem. Soc. Astron. Italiana, 83, 230
- Canuto, V., Lodenguai, J., & Ruderman, M. 1971, Phys. Rev. D, 3, 2303
- Cash, W. 1979, ApJ, 228, 939
- Chashkina, A., Abolmasov, P., & Poutanen, J. 2017, ArXiv e-prints
- Christodoulou, D. M., Laycock, S. G. T., Yang, J., & Fingerman, S. 2016, ApJ, 829, 30
- Clark, G., Doxsey, R., Li, F., Jernigan, J. G., & van Paradijs, J. 1978, ApJ, 221, L37
- Corbet, R. H. D., Edge, W. R. T., Laycock, S., et al. 2003, in Bulletin of the American Astronomical Society, Vol. 35, AAS/High Energy Astrophysics Division #7, 629
- Cowley, A. P. & Schmidtke, P. C. 2004, AJ, 128, 709
- Davies, S. R. 1990, MNRAS, 244, 93
- De Marco, B. & Ponti, G. 2016, ApJ, 826, 70
- den Herder, J. W., Brinkman, A. C., Kahn, S. M., et al. 2001, A&A, 365, L7
- Díaz Trigo, M., Migliari, S., Miller-Jones, J. C. A., & Guainazzi, M. 2014, A&A, 571, A76

- Díaz Trigo, M., Parmar, A. N., Boirin, L., Méndez, M., & Kaastra, J. S. 2006, *A&A*, 445, 179
- Dickey, J. M. & Lockman, F. J. 1990, *ARA&A*, 28, 215
- Dotan, C. & Shaviv, N. J. 2011, *MNRAS*, 413, 1623
- Edge, W. R. T., Coe, M. J., Corbet, R. H. D., Markwardt, C. B., & Laycock, S. 2004, *The Astronomer's Telegram*, 225
- Endo, T., Nagase, F., & Mihara, T. 2000, *PASJ*, 52, 223
- Evans, P. A., Beardmore, A. P., Page, K. L., et al. 2007, *A&A*, 469, 379
- Fürst, F., Walton, D. J., Harrison, F. A., et al. 2016, *ApJ*, 831, L14
- Ghosh, P. & Lamb, F. K. 1979a, *ApJ*, 232, 259
- Ghosh, P. & Lamb, F. K. 1979b, *ApJ*, 234, 296
- Ghosh, P. & Lamb, F. K. 1992, in *X-Ray Binaries and the Formation of Binary and Millisecond Radio Pulsars*, 487–510
- Ghosh, P., Pethick, C. J., & Lamb, F. K. 1977, *ApJ*, 217, 578
- Gilfanov, M. 2010, in *Lecture Notes in Physics*, Berlin Springer Verlag, Vol. 794, *Lecture Notes in Physics*, Berlin Springer Verlag, ed. T. Belloni, 17
- Graczyk, D., Pietrzyński, G., Thompson, I. B., et al. 2014, *ApJ*, 780, 59
- Gregory, P. C. & Lored, T. J. 1996, *ApJ*, 473, 1059
- Hickox, R. C., Narayan, R., & Kallman, T. R. 2004, *ApJ*, 614, 881
- Hickox, R. C. & Vrtilik, S. D. 2005, *ApJ*, 633, 1064
- Ikhsanov, N. R. & Mereghetti, S. 2015, *MNRAS*, 454, 3760
- Israel, G. L., Belfiore, A., Stella, L., et al. 2017a, *Science*, 355, 817
- Israel, G. L., Papitto, A., Esposito, P., et al. 2017b, *MNRAS*, 466, L48
- Jahoda, K., Markwardt, C. B., Radeva, Y., et al. 2006, *ApJS*, 163, 401
- Kaminker, A. D., Fedorenko, V. N., & Tsygan, A. I. 1976, *Soviet Ast.*, 20, 436
- Kennea, J. A., Coe, M. J., Evans, P. A., et al. 2016, *The Astronomer's Telegram*, 9362
- King, A. & Lasota, J.-P. 2016, *MNRAS*, 458, L10
- King, A., Lasota, J.-P., & Kluźniak, W. 2017, *MNRAS*, 468, L59
- Klochkov, D., Staubert, R., Santangelo, A., Rothschild, R. E., & Ferrigno, C. 2011, *A&A*, 532, A126
- Klus, H., Ho, W. C. G., Coe, M. J., Corbet, R. H. D., & Townsend, L. J. 2014, *MNRAS*, 437, 3863
- Kolehmainen, M., Done, C., & Díaz Trigo, M. 2014, *MNRAS*, 437, 316
- Koliopanos, F. & Gilfanov, M. 2016, *MNRAS*, 456, 3535
- Koliopanos, F., Vasilopoulos, G., Gobet, O., et al. 2017, *A&A* submitted, 0, 0
- Kosec, P., Pinto, C., Fabian, A. C., & Walton, D. J. 2018, *MNRAS*, 473, 5680
- Krtićka, J., Owocki, S. P., & Meynet, G. 2011, *A&A*, 527, A84
- Kuehnel, M., Kretschmar, P., Nespoli, E., et al. 2015, in *Proceedings of "A Synergistic View of the High Energy Sky" - 10th INTEGRAL Workshop (INTEGRAL 2014). 15-19 September 2014. Annapolis, MD, USA. Published online at <http://pos.sissa.it/cgi-bin/reader/conf.cgi?confid=228>, id.78, 78*
- La Barbera, A., Burderi, L., Di Salvo, T., Iaria, R., & Robba, N. R. 2001, *ApJ*, 553, 375
- La Palombara, N. & Mereghetti, S. 2006, *A&A*, 455, 283
- La Palombara, N., Sidoli, L., Pintore, F., et al. 2016, *MNRAS*, 458, L74
- Larsson, S. 1996, *A&AS*, 117, 197
- Lodenquai, J., Canuto, V., Ruderman, M., & Tsuruta, S. 1974, *ApJ*, 190, 141
- Lyubarskii, Y. E. & Syunyaev, R. A. 1988, *Soviet Astronomy Letters*, 14, 390
- Manousakis, A., Walter, R., Audard, M., & Lanz, T. 2009, *A&A*, 498, 217
- McBride, V. A., Coe, M. J., Negueruela, I., Schurch, M. P. E., & McGowan, K. E. 2008, *MNRAS*, 388, 1198
- Mészáros, P. 1992, *High-energy radiation from magnetized neutron stars*.
- Meszáros, P. & Nagel, W. 1985, *ApJ*, 299, 138
- Mushtukov, A. A., Suleimanov, V. F., Tsygankov, S. S., & Ingram, A. 2017, *MNRAS*
- Mushtukov, A. A., Suleimanov, V. F., Tsygankov, S. S., & Poutanen, J. 2015, *MNRAS*, 454, 2539
- Nagel, W. 1981, *ApJ*, 251, 288
- Negoro, H., Nakajima, M., Kawai, N., et al. 2016, *The Astronomer's Telegram*, 9348
- Ng, C., Díaz Trigo, M., Cadolle Bel, M., & Migliari, S. 2010, *A&A*, 522, A96
- Okazaki, A. T., Hayasaki, K., & Moritani, Y. 2013, *PASJ*, 65, 41
- Paul, B., Agrawal, P. C., Rao, A. R., & Manchanda, R. K. 1996, *Bulletin of the Astronomical Society of India*, 24, 729
- Paul, B., Agrawal, P. C., Rao, A. R., & Manchanda, R. K. 1997, *A&A*, 319, 507
- Pietrzyński, G., Graczyk, D., Gieren, W., et al. 2013, *Nature*, 495, 76
- Pinto, C., Alston, W., Soria, R., et al. 2017a, *MNRAS*, 468, 2865
- Pinto, C., Fabian, A., Middleton, M., & Walton, D. 2017b, *Astronomische Nachrichten*, 338, 234
- Pinto, C., Middleton, M. J., & Fabian, A. C. 2016, *Nature*, 533, 64
- Pintore, F., Zampieri, L., Stella, L., et al. 2017, *ApJ*, 836, 113
- Postnov, K. A., Gornostaev, M. I., Klochkov, D., et al. 2015, *MNRAS*, 452, 1601
- Pottschmidt, K., Ballhausen, R., Wilms, J., et al. 2016, *The Astronomer's Telegram*, 9404
- Poutanen, J., Lipunova, G., Fabrika, S., Butkevich, A. G., & Abolmasov, P. 2007, *MNRAS*, 377, 1187
- Poutanen, J., Mushtukov, A. A., Suleimanov, V. F., et al. 2013, *ApJ*, 777, 115
- Ramsay, G., Zane, S., Jimenez-Garate, M. A., den Herder, J.-W., & Hailey, C. J. 2002, *MNRAS*, 337, 1185
- Rea, N., Israel, G. L., Di Salvo, T., Burderi, L., & Cocozza, G. 2004, *A&A*, 421, 235
- Reig, P. 2011, *Ap&SS*, 332, 1
- Reig, P. & Nespoli, E. 2013, *A&A*, 551, A1
- Reig, P., Torrejón, J. M., & Blay, P. 2012, *MNRAS*, 425, 595
- Romanova, M. M., Ustyugova, G. V., Koldoba, A. V., & Lovelace, R. V. E. 2004, *ApJ*, 610, 920
- Schönherr, G., Wilms, J., Kretschmar, P., et al. 2007, *A&A*, 472, 353
- Schulz, N. S., Canizares, C. R., Lee, J. C., & Sako, M. 2002, *ApJ*, 564, L21
- Shakura, N. I. & Sunyaev, R. A. 1973, *A&A*, 24, 337
- Shimura, T. & Takahara, F. 1995, *ApJ*, 445, 780
- Sibgatullin, N. R. & Sunyaev, R. A. 2000, *Astronomy Letters*, 26, 699
- Staubert, R., Shakura, N. I., Postnov, K., et al. 2007, *A&A*, 465, L25
- Sturm, R., Haberl, F., Pietsch, W., et al. 2013, *A&A*, 558, A3
- Suleimanov, V. F., Lipunova, G. V., & Shakura, N. I. 2007, *Astronomy Reports*, 51, 549
- Sunyaev, R. A. & Titarchuk, L. G. 1980, *A&A*, 86, 121
- Townsend, L. J., Kennea, J. A., Coe, M. J., et al. 2017, *arXiv:1701.02336*
- Trümper, J. E., Dennerl, K., Kylafis, N. D., Ertan, Ü., & Zezas, A. 2013, *ApJ*, 764, 49
- Tsygankov, S. S., Doroshenko, V., Lutovinov, A. A., Mushtukov, A. A., & Poutanen, J. 2017, *arXiv:1702.00966*
- Tsygankov, S. S., Lutovinov, A. A., Churazov, E. M., & Sunyaev, R. A. 2007, *Astronomy Letters*, 33, 368
- Tsygankov, S. S., Lutovinov, A. A., & Serber, A. V. 2010, *MNRAS*, 401, 1628
- Udalski, A., Szymański, M. K., & Szymański, G. 2015, *Acta Astron.*, 65, 1
- Vasco, D., Klochkov, D., & Staubert, R. 2011, *A&A*, 532, A99
- Vasilopoulos, G., Haberl, F., Delvaux, C., Sturm, R., & Udalski, A. 2016, *MNRAS*, 461, 1875
- Vasilopoulos, G., Haberl, F., & Maggi, P. 2017, *MNRAS* accepted, 0, 0
- Vasilopoulos, G., Haberl, F., Sturm, R., Maggi, P., & Udalski, A. 2014, *A&A*, 567, A129
- Vasilopoulos, G., Maggi, P., Haberl, F., et al. 2013, *A&A*, 558, A74
- Vasilopoulos, G. & Petropoulou, M. 2016, *MNRAS*, 455, 4426
- Verner, D. A., Ferland, G. J., Korista, K. T., & Yakovlev, D. G. 1996, *ApJ*, 465, 487
- Walter, R. & Ferrigno, C. 2016, *arXiv:1608.06530*
- Walter, R., Lutovinov, A. A., Bozzo, E., & Tsygankov, S. S. 2015, *A&A* Rev., 23, 2
- Wang, Y.-M. & Frank, J. 1981, *A&A*, 93, 255
- Watson, M. G., Schröder, A. C., Fyfe, D., et al. 2009, *A&A*, 493, 339
- Weng, S.-S., Ge, M.-Y., Zhao, H.-H., et al. 2017, *ApJ*, 843, 69
- White, N. E., Swank, J. H., & Holt, S. S. 1983, *ApJ*, 270, 711
- Wilms, J., Juett, Schulz, & Nowak. 2011, *ApJ*
- Wilms, J., Allen, A., & McCray, R. 2000, *ApJ*, 542, 914
- Wilson, C. A., Finger, M. H., & Camero-Arranz, A. 2008, *ApJ*, 678, 1263